Title: Bacterial infection reshapes monocyte and macrophage ontogeny at the CNS borders

Authors: Vitka Gres[1], Florens Lohrmann[1,2], Vidmantė Fuchs[3,4], Jana Neuber[1], Zohreh Mansoori Moghadam[1], Anne K. Lösslein[1,6], Lance F. P. Bosch[1,3,4], Tiago Figueiral-Martins[1,3,7], Sebastian Baasch[1,8], David Obwegs[3,12], Gianni Monaco[4,9,10], Julia Henschel[3,4], Klaus P. Knobeloch[4,5], Marco Prinz[4,5], Steffen Jung[11], Katrin Kierdorf[1,4,5], Sagar[12], Julia Kolter[1], Daniel Erny[4†], Philipp Henneke[1,5, 13*†]

Affiliations:

[1]Institute for Infection Control and Prevention, Medical Center and Faculty of Medicine, University of Freiburg; Freiburg, Germany.

[2]Department of Pediatrics and Adolescent Medicine, Medical Center and Faculty of Medicine, University of Freiburg; Freiburg, Germany.

[3]Faculty of Biology, University of Freiburg; Freiburg, Germany.

[4]Institute of Neuropathology, Faculty of Medicine, University of Freiburg; Freiburg, Germany.

[5]Centre for Integrative Biological Signalling Studies (CIBSS), University of Freiburg; Freiburg, Germany.

[6]Institute of Medical Microbiology and Hygiene, Medical Center and Faculty of Medicine, University of Freiburg; Freiburg, Germany.

[7]Spemann Graduate School of Biology and Medicine (SGBM), University of Freiburg; Freiburg, Germany.

[8]Freiburg Institute for Advanced Studies (FRIAS), University of Freiburg; Freiburg, Germany.

[9]Single-Cell Omics Platform Freiburg, Faculty of Medicine, University of Freiburg; Freiburg, Germany.

[10]Institute for Transfusion Medicine and Gene Therapy, Medical Center, University of Freiburg; Freiburg, Germany.

[11] Department of Immunology and Regenerative Biology, Weizmann Institute of Science; Rehovot, Israel.

[12] Department of Medicine II, University Medical Center, Medical Faculty, University of Freiburg; Freiburg, Germany.

[13] Centre for Chronic Immunodeficiency, University Medical Center, Medical Faculty, University of Freiburg; Freiburg, Germany.

[†]Equal contribution

[*]Correspondence: philipp.henneke@uniklinik-freiburg.de

Abstract:
Macrophages in the meninges contribute to immune defense of the central nervous system (CNS), yet their site-specific origin and function remain poorly understood. Using an intravenous model of streptococcal meningoencephalitis in mice, we found bacteria predominantly in the leptomeninges and dura. Nevertheless, monocyte infiltration into the leptomeninges and parenchyma strongly correlated with disease severity. In the dura, infection triggered activation and loss of resident macrophages, followed by rapid engraftment of inflammatory monocytes that transiently replenished the macrophage niche. Under homeostasis, dural monocytes were supplied CCR2-independently from adjacent skull bone marrow. During infection, this local source was insufficient, necessitating recruitment from peripheral bone marrow. Infection further reshaped monocyte ontogeny, increasing monocyte–dendritic cell progenitor–derived monocytes, which expressed higher MHC-II and persisted in the brain alongside $CD4^+$ T cells during resolution. Together, these findings reveal dynamic, compartment-specific remodeling of monocyte recruitment and differentiation across CNS borders during bacterial meningoencephalitis.

One Sentence Summary: Streptococcal meningoencephalitis disrupts homeostatic, skull bone marrow-derived monocyte and macrophage trajectories in the dura.

Main Text:

INTRODUCTION

Bacterial meningoencephalitis is a devastating disease that affects millions of people each year. Group B streptococcus (*Streptococcus agalactiae*, GBS) is a common colonizer of the gastrointestinal and urogenital tract, but also a leading cause of neonatal meningoencephalitis. GBS poses a particular risk to patients with diabetes mellitus, pregnant women, the elderly, and immunocompromised people (*1*). GBS meningoencephalitis has a mortality rate of up to 10%, and surviving patients often suffer from neurological sequelae (*2*, *3*).

The integrity of the brain is protected by anatomical barriers that ensure the controlled passage of molecules from the periphery into the central nervous system (CNS). The choroid plexus, the perivascular space along the vessels, and the meninges harbor populations of macrophages, together called CNS-associated macrophages (CAM). CAM play a crucial role in maintaining CNS homeostasis, but also provide neuroprotection in many pathologies (*4*–*7*). Anatomically, the meninges consist of three layers – dura mater, as well as arachnoid and pia mater (leptomeninges) (*8*). The dura harbors a complex immunologic landscape, includingdiverse subsets of the most abundant population – dural macrophages (*9*).

Dural sinuses, which drain venous blood, are sites of antigen sampling and presentation (*10*). The dura is connected to the skull marrow by ossified channels, which provide a direct migration route for monocytes, neutrophils and B cells (*11*, *12*). Cerebrospinal fluid transports bacteria from the dura to the skull marrow when bacteria like *Streptococcus pneumoniae* are injected into the cisterna magna (*13*). However, the dynamics of the dura–skull marrow immune axis in blood-borne bacterial infection remain unclear. In contrast to the dura, the brain parenchyma contains only one resident immune population in steady state – microglia. In a healthy brain, microglia hardly ever encounter peripheral immune cells such as neutrophils, T cells or monocytes. In contrast, neuroinflammatory diseases, e.g., multiple sclerosis (*14*) or ischemic stroke (*15*) can disrupt the blood-brain barrier and promote leukocyte infiltration, contributing to microglia activation and disease exacerbation. During GBS infection in the CNS, neuroimmune communication appears to be crucial. Microglia may exacerbate immunopathology in infection, for example, by producing nitric oxide that promotes neuronal death (*16*). Conversely, trigeminal ganglion nociceptors in the dura dampen the response of dural macrophages through CGRP-RAMP1 signaling, which leads to increased spread of bacteria into the brain parenchyma (*17*). Hence, the cross-talk of the immune compartments in the CNS parenchyma and interfaces seem to play major roles in disease progression and outcome. However, the precise immune cell dynamics in the CNS and its borders during streptococcal meningoencephalitis remain poorly understood.

Here, we investigated the discrete immune responses of microglia, dural macrophages, and infiltrating monocytes in streptococcal meningoencephalitis caused by hematogenous spread. We found that dural macrophages are positioned at the primary interface of the infection, initiating immune activation. Infiltrating Ly6C^{hi} monocytes actively replenished resident dural macrophages and were imprinted by their cellular origin. Moreover, monocyte invasion into the adjacent CNS

parenchyma was associated with adverse infection outcome. Thus, streptococcal infection induces fundamental ontogenetic and functional changes in tissue-resident macrophages of the CNS interfaces, and the recruitment pathways and differentiation dynamics of migrating monocytes are linked to disease progression.

RESULTS

The meninges serve as a reactive CNS barrier during hematogenous GBS infection

Previous studies on the immune responses in bacterial meningoencephalitis in mice typically relied on disease models in which the pathogen was directly injected into the cisterna magna (*13*, *18*, *19*), therefore circumventing the effects of peripheral immune activation and systemic bacterial dissemination on CNS inflammation. In streptococcal meningoencephalitis, mucosal colonization usually precedes CNS infection, and bacterial dissemination via the blood is often observed (*20*). To investigate the systemic dissemination of GBS and its capacity to invade the CNS, we intravenously injected wild type (*Wt*) mice with $5x10^7$ colony forming units (CFU) of the serotype III hypervirulent BM110 GBS strain, which is linked to neonatal meningoencephalitis in humans (*21*, *22*). The infection spread rapidly and the overall fitness of infected mice drastically declined until 3 days post-infection (dpi) when mice lost around 20% of their body weight, leading to termination of the experiments (Fig. S1A). We therefore focused on the 2 dpi timepoint, at which we observed bacterial presence in blood, brain lysates including leptomeninges, dura mater, liver, skull and femur (Fig 1A). In agreement with previous data on GBS sepsis (*23*), interleukin (IL)-6 levels in the plasma (Fig. S1B) as well as tumor necrosis factor (TNF), IL-1β and interferon (IFN)-β in the brain lysates of infected mice were substantially increased (Fig. S1C).

Detailed spatial mapping revealed that GBS dissemination into the brain parenchyma was rare, indicating that CNS border tissues effectively restricted bacterial entry (Fig. 1B, S1D). Whereas control brains and dura lacked a detectable bacterial signal (Fig. S2A–C), infection resulted in limited bacterial presence in the choroid plexus and marked accumulation in the leptomeninges and dura mater (Fig. 1B–E, S1D). This containment implied active immune responses, prompting us to next examine immune cell recruitment to the brain in response to GBS invasion. Flow cytometry analysis showed an influx of $Ly6C^{hi}$ monocytes into the brain, including the leptomeninges, while neutrophil numbers were only marginally increased (Fig.1F, S1E). Monocyte influx positively correlated with bacterial burden in the brain (including leptomeninges) ($r > 0.9$), and in the mice with severe infections, monocyte counts increased more than 50-fold compared to less affected mice (Fig.1G). In contrast, the dura of GBS-infected mice showed an increase in both monocyte and neutrophil counts (Fig.1H). Moreover, numbers of resident dural macrophages in infection were reduced, both within the sinuses and in extra-sinus area (Fig.1H, I, J). While dural macrophages have been previously characterized as $MHC\text{-}II^{hi}$ or $MHC\text{-}II^{low}$, both subsets declined proportionally during infection, with unchanged subset frequencies (Fig.S1F,G).

To spatially validate both GBS localization and bone marrow-derived myeloid cell influx, we utilized $Ms4a3^{Cre};R26^{Tomato}$ mice, in which granulocyte-monocyte progenitors (GMP) and their progeny (including monocytes and neutrophils) are labeled. Coronal head sections from infected $Ms4a3^{Cre};R26^{Tomato}$ mice showed robust accumulation of $Tomato^+$ myeloid cells in both dura and

leptomeninges, co-localizing with GBS foci (Fig.1K, S2D-F). Moreover, $CD45^+$ immune cell infiltration was observed both at bacteria-enriched border regions, e.g., leptomeninges (Fig. S2G, H, J), but also within the relatively less affected brain parenchyma (Fig. S2G, H, I).

Collectively, these data show a compartmentalized pattern of GBS dissemination drastically affecting the immune cell composition of the meninges and the brain. Considering that tissue resident macrophages are the first responders in infection, we sought to investigate the transcriptional changes of CNS resident macrophage populations upon the bacterial challenge. Specifically, we focused on two distinct myeloid populations: dural macrophages and microglia. To selectively target long-lived dural macrophages, we employed *Mrc1*^{CreERT2}*;R26*^{Tomato} mice with tamoxifen (TAM)-induced labeling performed eight weeks prior to infection followed by bulk RNA sequencing (RNA-seq) 2 dpi (Fig.1L). This timeline enabled us to distinguish resident dural macrophages from newly recruited monocyte-derived cells in the dura, while also allowing us to discriminate between microglia and other CAM (Fig.S1H, I).

Principal component analysis (PCA) of RNA-seq data showed distinct clustering of the isolated populations. Whereas microglia from control and infected mice clustered closely together, dural macrophages from infected and uninfected mice showed a distinct gene expression profile (Fig 1M). In line with our previous data on peripheral GBS infection (*24*), many of the upregulated differentially expressed genes (DEG) in dural macrophages and microglia after GBS infection were associated with type I IFN signaling and with the defense response to bacteria, e.g., *Oasl2, Irf7, Usp18, Fcgr4, Gbp2, Ifit1, Oas3, Isg15,* and *Ifi44,* implying the existence of a common type I IFN-driven response of tissue resident macrophages to GBS (Fig.1N). While both populations mounted a similar core transcriptional response, the overall magnitude of gene induction expressed as $\log_2$(fold change) was higher in dural macrophages compared to microglia (Fig.1O). In summary, a strong inflammatory response and reduction of dural macrophages, coupled with a monocyte and neutrophil influx identifies the dura as a highly reactive immune interface in response to GBS infection.

Loss of dural macrophages triggers compensatory monocyte differentiation

Previous reports have shown that neuroinflammatory conditions such as infection or stroke enable monocyte engraftment into both the parenchyma and in the meninges (*18*, *25–27*). We therefore asked whether the changes in resident dural macrophages and microglia described above were accompanied by infection-driven monocyte-to-macrophage differentiation. We first examined homeostatic monocyte-macrophage turnover using the *Cxcr4*^{CreERT2}*;R26*^{Tomato} mouse model, in which TAM induction labels hematopoietic stem cell (HSC)-derived cells, for up to six months (*28*). In steady state, microglia are established early in embryonic development and do not receive substantial input from peripheral monocytes (*29*, *30*) and thus remained unlabeled throughout the experiment. In contrast, dural macrophages showed a gradual replacement by circulating monocytes, reaching up to 24% after 8 weeks and 45% at 16 weeks (Fig. S3A). Next, we assessed whether the infection altered dural macrophage and microglia differentiation dynamics by analyzing *Cxcr4*^{CreERT2}*;R26*^{Tomato} mice 2 dpi that were treated with TAM 8 weeks prior (Fig. 2A). We did not detect $Tomato^+$ microglia in the brain or an increased frequency of $CD206^+Ly6c^{neg}$ $Tomato^+$ dural macrophages in infection (Fig. 2B). In the dura, however, GBS infection induced a

marked expansion of late-Mo/early-macrophage cells co-expressing Ly6C and CD206 (Fig. 2C, D). These macrophages were of HSC origin (Fig. 2E) and, unlike Ly6C$^+$ dural monocytes, upregulated MHC-II (Fig. 2F). Therefore, they likely represented a transient monocyte-to-macrophage differentiation stage that facilitates repopulation of the dural macrophage compartment during infection, compensating for infection-driven loss.

To further explore changes of myeloid populations in depth, we performed single-cell transcriptional analysis on sorted CD45$^+$CD11b$^+$ myeloid cells from control and GBS-infected dura (Fig. 2G). Using unbiased hierarchical clustering analysis, we were able to distinguish 12 distinct cell clusters (Fig. 2H, S3B). Within the macrophagecompartment, all dural macrophages clusters expressed their canonical genes, including *Mrc1*, *Pf4*, *Cd68*, and *Cx3cr1*, but each exhibited some distinct transcriptional features (Fig. S3B). Cluster 0 was enriched for type I IFN–responsive genes such as *Oasl1* and *Cxcl10*. Cluster 2 showed elevated expression of MHC-II–associated genes. Cluster 3 was marked by higher *Cbr2* expression, while cluster 4 was characterized by increased *Lyve1* (Fig. S3B,C). Furthermore, we identified three monocyte populations: classical monocytes, patrolling monocytes characterized by higher *Itgal* expression, and a distinct population that emerged specifically during infection and was virtually absent under homeostatic conditions (cluster 5) (Fig. 5H, S3B). We therefore refer to this population as infection-associated monocytes, which exhibited elevated expression of antimicrobial and inflammatory genes, including *Nos2, Rsad2, Mif, Cfb, Cxcl9,* and *Ccl5,* compared to the other monocyte clusters (Fig. S3D).

Consistent with previous observations, a relative decrease of percentage in macrophage clusters (0,2,3,4, Fig. 2I) and an increase of percentage in neutrophil (1) and monocyte (5,6,7) clusters (Fig. 2J) correlated with the brain bacterial burden (Fig. S3E). Dural macrophages, particularly clusters 0 and 3, upregulated necroptosis regulators *Mlkl, Ripk1* and *Zbp1*, indicating that their loss may involve necroptotic death pathways reported in other bacterial infections (Fig. S3F)(*31*, *32*). Conversely, the expression of *Mrc1*, *H2-Ab1* and *Cd74* in monocyte cluster 5 increased proportionally to the bacterial burden (Fig. 2K), consistent with accelerated monocyte-to-macrophage differentiation in response to infection-driven macrophage depletion (Fig. 2C–F).

Next, to functionally validate the rapid monocyte-to-macrophage differentiation observed during infection, we adoptively transferred monocyte progenitors (MP) isolated from *β-actin-GFP* mice into either infected or control mice (Fig. 2L, S3G). In infected mice, we detected robust engraftment of GFP$^+$ donor cells in the dura, with preferential accumulation in sinus-associated regions (Fig. S3H). A subset of these cells upregulated CD206 and acquired an ameboid morphology, consistent with acquisition of macrophage-like features (Fig. 2M, N). Overall, infection triggered a broad diversification of monocyte states and accelerated their differentiation into macrophages, highlighting a remarkable degree of lineage plasticity within the inflamed dura.

Distinct monocyte sources support dural immunity in steady state and infection

Having established that infection induces extensive monocyte recruitment into the dura and the brain, we next wanted to determine their functional role in streptococcal infection. Since CCR2 is considered a key driver of monocyte mobilization from the bone marrow (*33*), we performed GBS

infection in *Ccr2*$^{-/-}$ mice. At 2 dpi, bacterial loads were similar between GBS-infected *Wt* and *Ccr2*$^{-/-}$ mice in the periphery and the brain, including leptomeninges (Fig. S4A), indicating that infiltrating Ly6C^{hi} monocytes neither play a critical role in early bacterial control, nor were directly involved in bacterial dissemination into the CNS. In addition, steady state monocyte numbers in the dura were similar between *Ccr2*$^{-/-}$ and *Wt* mice (Fig. 3A), consistent with the observation that dural monocytes express lower levels of *Ccr2* than circulating monocytes (Fig. S4B). In contrast, we did not observe a notable monocyte influx in *Ccr2*$^{-/-}$ mice in the dura or in the brain (including leptomeninges) upon infection, compared to *Wt* mice (Fig. 3A, 3B). Lack of monocytes was not compensated for by higher numbers of infiltrating granulocytes during GBS infection, as *Ccr2*$^{-/-}$ mice showed even lower dural neutrophil numbers than *Wt* mice (Fig. S4C). These findings indicate that, unlike classical inflammatory monocyte trafficking, homeostatic monocyte access to the dura occurs largely through a CCR2-independent mechanism, whereas CCR2 becomes critical during infection-induced monocyte mobilization. The persistence of monocytes in the dura of *Ccr2*$^{-/-}$ mice consequently raised the question of their anatomical origin.

Previous reports have highlighted the skull marrow as a primary source for monocytes and B cells replenishing the dura in homeostasis (*12*, *34*). In order to evaluate the contribution of the adjacent skull marrow during GBS infection, we transplanted bone marrow from either *Cx3cr1*$^{+/gfp}$ or *β-Actin-GFP* mice, and in both cases, monocytes and monocyte-derived dural macrophages coming from the donor were GFP-labeled. Recipient mice were subjected to either full body irradiation or head-shielded irradiation, enabling us to discriminate between local (skull) versus peripheral (femur) bone marrow contribution to the dural monocyte pool (Fig. 3C). In fully irradiated mice, Ly6C^{hi} monocyte populations reached close to 100% chimerism after 8 weeks post-transplantation in all assessed compartments (Fig. 3D, S4D). In contrast, femurs of head-shielded mice showed incomplete chimerism as previously reported (*35*), while the skull marrow, which was predominantly protected by head-shielding, had less contribution of donor-derived cells (Fig. 3D, S4D).

To understand donor-cell integration dynamics in dura and the bone marrow sites, we calculated relative chimerism rates by comparing the ratios of GFP^{+} monocytes from dura to skull bone marrow or femur bone marrow. In fully irradiated mice, there was no difference in monocyte populations at the three sites (Fig. 3E, S4E, S4F). In head-shielded mice, relative chimerism showed that the dural monocytes closely mirrored the skull marrow chimerism (Fig. 3E). In contrast, femur monocytes had almost two times higher engraftment compared to dural monocytes (Fig. 3E). Considering the relatively short lifespan of Ly6C^{hi} monocytes (*36*), these results strongly suggested that, in steady state, the skull marrow dominated over peripheral bone marrow as monocyte reservoir for the dura. Moreover, whereas more than 75% of dural macrophages were replaced by donor-derived cells following full body irradiation, we found only 5% donor-derived dural macrophages 8 weeks post-irradiation with head-shielding (Fig. 3F, G). For comparison, fate-mapping experiments indicate that ~24% of dural macrophages are normally replaced by monocytes over this timeframe (Fig. S3A), suggesting that dural macrophages replacement is largely supported by skull-derived monocytes in this setting.

To determine whether the skull bone marrow supply of monocytes persists during infection, we infected head shielded chimeras 8 weeks after bone marrow transplantation with GBS (Fig. 3H). The chimerism of the skull and femur monocytes remained similar in infected and non-infected mice (Fig 3K, S4H). In contrast, the percentage of donor-derived Ly6C^{hi} monocytes in the dura

increased upon infection, indicating an accelerated recruitment from other (non-skull) bone marrow sources (Fig. 3I, 3J, 3K, S4H, S4I). While monocytes were not detectable in the control brain, infiltrating monocytes showed a comparable chimerism to monocytes in the dura and femur upon infection in head-shielded mice, suggesting the peripheral influx in both compartments (Fig. S4H). Therefore, the accelerated replacement dynamics under infection indicated an extensive recruitment of monocytes from peripheral sources, without a preferential anatomical bone marrow niche (Fig. 3I). Additionally, the acceleration of dural macrophage replacement by donor-derived monocyte progenitors pointed to a faster monocyte-to-macrophage differentiation in the acute infection (Fig. 3L). Together, these results suggest that the previously proposed CCR2-independent homeostatic replenishment of dura monocytes from the skull marrow does not suffice to meet the highly increased demand for monocytes in streptococcal meningoencephalitis. In addition and as reported before (*35*), irradiation let to a minor engraftment of donor-derived cells to the brain microglial pool, which was highly reduced in head shielded chimera (Fig. S4G, S4J). Donor-derived cells in the infected head-shielded chimeras were mostly localized in the leptomeninges and were not observed integrating into the microglial pool (Fig. S4J).

Given these dynamic shifts in monocyte sourcing, we next investigated whether GBS infection alters myelopoiesis within the skull and femoral bone marrow compartments. Previous studies have demonstrated that bacterial infections can skew haematopoiesis toward emergency myelopoiesis (*37*). In our model, GBS was detected in both skull and femur bone marrow, suggesting direct bacterial engagement with hematopoietic niches (Fig. 3M, S4K). All analyzed progenitor populations showed a decreasing trend during infection in both skull and femoral bone marrow (Fig. 3 N-R), including common myeloid progenitor (CMP), with the most pronounced reduction observed in GMP compartment (Fig. 3O, S5A). In addition, monocyte progenitors and monocyte–dendritic progenitors (MDP) were reduced in the skull bone marrow, while only modestly affected in the femur (Fig. 3P, Q, S5B). Despite these changes at the progenitor level, monocyte numbers remained stable in both compartments during infection (Fig. 3R). These findings indicate that GBS infection imposes distinct pressures on myeloid populations within different bone marrow reservoirs. While both sites participate in emergency myelopoiesis, the skull marrow appears particularly vulnerable to progenitor depletion, potentially reflecting its rapid mobilization of monocytes to the connected dura.

GBS infection reprograms monocyte ontogeny toward MDP-derived lineages

Having observed a site-specific depletion of myeloid progenitor subsets prompted us to investigate whether GBS infection alters the ontogeny of monocytes originating from these sites. Under steady-state conditions, most monocytes arise from GMP derived from CMP, although a smaller subset can develop from MDP (*38–40*)(Fig. 4A). To distinguish between these developmental pathways, we utilized *Ms4a3*^{Cre}*;R26*^{Tomato} reporter mice, in which GMP-derived monocytes (GMP-Mo) and neutrophils are irreversibly labeled (*39*), whereas MDP-derived monocytes (MDP-Mo) remain Tomato-negative. During GBS infection, MDP-Mo frequencies increased in both skull and femur bone marrow (Fig. 4B), however, this shift was more pronounced in the skull, consistent with the site-specific progenitor depletion due to emergency myelopoiesis, as described above (Fig. 3N-R). Importantly, neutrophils (Fig. S6A) and GMP-derived monocyte progenitors, such as

common monocyte progenitor (cMoP), remained labeled in both skulls and femurs during homeostasis and infection, confirming that altered Tomato labeling reflected genuine changes in monocyte ontogeny rather than infection-induced recombination artifacts (Fig. S6C). Conversely, MDPs remained Tomato^{neg} (Fig. S6B,F). Furthermore, to independently verify monocyte labeling, we used *Cxcr4^{CreERT2};R26^{Tomato}* mice, in which TAM induction labels all HSC-derived cells (*28*) (Fig. 4A). Indeed, there was no difference in Tomato-labeling of monocytes in skull, femur or dura in infection (Fig. S6D, E).

Next, we analyzed if this ontogenic skewing was also evident in the dura during infection. Indeed, dural monocytes showed a marked increase in Tomato^{neg} MDP-Mo in *Ms4a3^{Cre};R26^{Tomato}* mice (Fig. 4C). Additionally, these MDP-Mo expressed CX3CR1 and displayed higher MHC-II levels compared to GMP-Mo (Fig. 4D, E). To further delineate differences of MDP-Mo and GMP-Mo in the infected dura, we performed single-cell RNA sequencing. Monocytes were gated as Lin^{neg}CD45^{+}CD11b^{+}Ly6C^{hi}CX3CR1^{+}, with Tomato used to distinguish between lineage origins (Fig. S6G). UMAP embedding did not separate the two lineages into discrete clusters, indicating substantial transcriptional convergence in the inflamed dural environment (Fig. 4F). Nonetheless, pseudo-bulk differential expression analysis revealed clear lineage-associated signatures, including higher MHC-II gene expression in MDP-Mo, consistent with flow cytometry (Fig. 4G). In total, 308 genes were differentially upregulated in MDP-Mo and 290 in GMP-Mo (Fig. 4H).

Comparison with a DEGs from published dataset of bulk RNA-seq from steady-state bone marrow–derived MDP-Mo and GMP-Mo (*40*) revealed partial overlap in signature (Fig. 4I, 4J, S6H, I, J). We then focused on DEGs that did not overlap with the steady-state dataset, reasoning that these might represent infection-associated transcriptional programs. Gene ontology analysis showed that GMP-Mo upregulated pathways related to mitochondrial respiration, oxidative phosphorylation, and antimicrobial defense, consistent with an energetically demanding inflammatory response (Fig. 4K). In contrast, MDP-Mo upregulated GO categories linked to immune system processes, cell differentiation, lymphocyte activation, and positive regulation of IL-17 production (Fig. 4L).

Given the identification of an infection-associated monocyte cluster in the dural myeloid scRNA-seq dataset (Fig. 2H–K), we next asked whether MDP-Mo and GMP-Mo could be distinguished within this population (Fig. S6K). Although unsupervised clustering did not resolve discrete subclusters, overlaying lineage-specific gene signatures revealed two largely non-overlapping expression patterns (Fig S6K). These feature plots are consistent with the coexistence of both monocyte lineages within cluster 5. Together, these findings indicate that GBS infection not only alters the quantity of monocytes recruited to the dura but also reshapes their developmental origins and transcriptional states, with skull bone marrow producing disproportionately more MDP-Mo under inflammatory pressure. This ontogenic reprogramming likely reflects differential stress imposed on bone marrow niches and may contribute to functional diversification of monocyte responses at the CNS interfaces during bacterial meningitis.

Post-infection monocyte ontogeny diverges between dura and brain

The infection-induced reprogramming of monocyte ontogeny, together with the high turnover of dural macrophages, raised the question of how the CNS myeloid landscape is restored once bacterial infection is resolved. Given that MDP-Mo expanded disproportionately during acute GBS infection in dura compared to the steady-state, we hypothesized that monocyte dynamics and their contribution to tissue macrophage pools might substantially change during the recovery phase. GBS meningitis is fatal in mice without treatment, mirroring the clinical situation in neonates. To model successful therapeutic intervention, we treated infected mice with ampicillin and azithromycin for two weeks, beginning at 2 dpi (Fig. 5A). Bacteria became undetectable in blood, brain and liver already at 7 dpi, confirming complete resolution of infection. By 7 dpi, monocyte and neutrophil numbers in the dura were only modestly elevated and had fully returned to baseline by 30 dpi (Fig. 5B, C). In contrast, dural macrophages expanded between 2 and 7 dpi (Fig. 5D), indicating a regenerative wave of macrophage replenishment during recovery. In the brain and leptomeninges, monocytes and neutrophils normalized by 7 dpi (Fig. 5E,F), although at this timepoint, monocytes persisted at low levels in the leptomeninges and parenchyma (Fig. 5E), suggesting ongoing immune activity beyond bacterial clearance.

Lineage analysis revealed that MDP-Mo follow distinct temporal dynamics in the dura versus the brain and leptomeninges. In the dura, MDP-Mo peaked at 2 dpi and rapidly declined to homeostatic levels during clearance (Fig. 5G, H). In contrast, in brain and leptomeninges MDP-Mo accumulated progressively and peaked at 7 dpi, constituting over 40% of the monocyte pool at this time (Fig. 5I, J). Because MDP-Mo expressed higher MHC-II than GMP-Mo and were enriched for GO terms associated with lymphocyte activation, we hypothesized that their delayed accumulation may reflect a role in antigen presentation and T cell activation. Indeed, $CD45^{+}CD11b^{neg}$ lymphocytes increased specifically in the brain and leptomeninges (Fig. S7A), but not the dura (Fig. S7B), at 7 dpi. Histological analysis of brain 7 dpi showed accumulation of $CD4^{+}$ T cells in proximity of MHC-II^{+} cells, of which most are found in CNS border areas such as the ventricles or the leptomeninges, but were also present in the brain parenchyma (Fig. 5K, L, S7D, E). Conversely, at 2 dpi and 30 dpi, we found very rare $CD4^{+}$ T cell incidence, mostly in leptomeningeal and ventricular regions (Fig. S7C). To further investigate whether the elevated MHC-II expression in MDP-Mo coincides with enhanced capacity for antigen presentation, we compared the antigen-presenting abilities of MDP-Mo and GMP-Mo. We isolated CD4 T cells from cervical lymph nodes (recipients of brain lymphatic drainage, (*41*)) of infected mice at 7 dpi and co-cultured them with MDP-Mo or GMP-Mo, which were stimulated with heat-fixed GBS for 2 h. After 18 h of co-culture, T cells expressed more IFN-γ and CD25 in culture with MDP-Mo, indicating that MDP-Mo possess superior T cell-activating properties (Fig. 5M, S7F,G).

Lastly, we asked whether GMP-Mo contribute to the restoration of dural macrophage niche. $Tomato^{+}$ dural macrophages in $Ms4a3^{Cre};R26^{Tomato}$ mice increased in the dura at 7 dpi but were back to steady state levels at 30 dpi, indicating they only contribute to the dural macrophage compartment transiently (Fig. 5N, O). Since MDP-Mo and MDP-derived macrophages cannot be fate-mapped with currently available tools, we assessed long-term dural macrophage maintenance using $Cxcr4^{CreERT2};R26^{Tomato}$mice induced one week before infection. $Tomato^{+}$ dural macrophage frequencies were indistinguishable between infected and control mice at 30 dpi (Fig. 5P), demonstrating that the dural macrophage niche is ultimately restored by long-lived tissue-resident macrophages rather than recruited monocyte progeny. Similarly, microglia remained $Tomato^{neg}$,

indicating that CNS parenchymal macrophages do not undergo substantial monocyte-derived replacement during or after GBS infection (Fig. S7H). Thus, while the dura and brain recruit distinct monocyte populations during infection and early recovery, both compartments ultimately revert to a resident cell–dominated homeostasis.

DISCUSSION

Acute streptococcal meningoencephalitis warrants major prevention efforts worldwide, due to its substantial consequences for cognition and motor function in surviving patients (*42*). The uniqueness of the disease in an individual's life is reflected by the long-standing concept of a largely immune-privileged brain, which—unlike other internal organs, such as the liver and kidneys—does not come into incidental contact with pathogens and peripheral immune cells (*43*). Accordingly, most mechanistic insights have focused on microglia, the resident immune cells of the CNS, largely because of the assumption that they are the primary mediators of immune defense within the CNS interior (*16*, *18*, *44*, *45*). In contrast, very little information is available on the role of CAM in this context, even though clinically, CNS borders play a central role in disease manifestation. This discrepancy is probably because until recently it was not possible to reliably distinguish between CAM and parenchymal microglia, and due to the paucity of robust rodent meningitis models in which bacteria are not injected directly into the CNS.

Lately, there has been increasing evidence that macrophages residing in brain barriers, particularly in the meninges, play an important role in various neuropathologies (*4*, *5*, *46*). In addition, the recent discovery of direct communication between the dura mater and skull bone marrow raises the question of the role of distinct bone marrow sites in disease (*11–13*, *47*, *48*). Accordingly, we have combined the latest tools in myeloid cell fate-mapping and multidimensional analysis with a mouse model in which streptococci circulate systemically before entering the CNS, as in a natural disease. In this model, we demonstrate that bacteria accumulate primarily in the leptomeninges and dura, with minimal penetration into the brain parenchyma, which aligns with emerging evidence that the meninges behave as a highly responsive immunological interface (*49*, *50*).

In contrast to perivascular and leptomeningeal macrophages, dural macrophages exhibit substantial turnover during steady state. This dependency becomes pronounced during infection, where resident macrophages are rapidly lost and replaced by monocyte-derived cells. The coordinated emergence of a Ly6C^{+}CD206^{+}MHC-II^{+} population suggests that recruited monocytes swiftly adopt macrophage-like properties within the inflamed dura. Rapid functional adaptation may therefore be critical for maintaining barrier integrity during bacterial invasion. Conversely, bacterial burden positively correlated to the loss of dural macrophages. It is conceivable that resident dural macrophages populations are the first responders in the early phase of infection, leading to cellular stress and ultimately, cell death. This observation is consistent with the so-called "macrophage disappearance reaction" which has been described in inflammation of the peritoneal cavity (*51*, *52*), the liver (*31*) and other tissues (*53*) and which might serve to initiate infection control. Infection-induced cell death of resident macrophages has also been found in the meninges in viral infection (*4*), accompanied by the engraftment of monocytes. Consistent with this, the upregulation of canonical necroptosis genes *Mlkl, Ripk1* and *Zbp1* in dural macrophage clusters in infection points to a likely mechanism of dural macrophage loss in our model.

The skull bone marrow has been identified as a local reservoir supplying the dura with myeloid cells in steady state (*12*), a feature which may be particularly relevant in the context of meningoencephalitis, when the demand for monocytes is high. Our data support a model in which skull-derived monocytes contribute substantially to dural macrophage renewal under homeostatic conditions. However, this local reservoir appears insufficient during infection. Instead, inflammatory conditions trigger a broader mobilization of monocytes, including recruitment from peripheral bone marrow sources. This shift suggests the existence of a recruitment threshold, beyond which local hematopoietic niches can no longer meet demand. Consistent with this, infection was associated with changes in skull marrow composition and the presence of bacteria within this compartment, indicative of emergency myelopoiesis. In parallel, we observed the accumulation of transcriptionally distinct, infection-associated monocytes in the dura mater, the recruitment of which depended on CCR2, in contrast to steady-state conditions.

Together, these findings point to a context-dependent reorganization of monocyte sourcing and trafficking during CNS infection. While skull marrow-derived monocytes dominate under homeostatic conditions, systemic cues appear to override predominantly local recruitment circuit during inflammation. The molecular signals governing homeostatic cell mobilization from the skull remain to be defined, but may involve other chemokines (e.g., CCL5), lipid mediators, or neuropeptides derived from dural innervation (*54*, *55*). It seems noteworthy that we did not find evidence that these infection-associated monocytes contributed to bacterial trafficking, as *Ccr2*$^{-/-}$ mice did not have a difference in bacterial load compared to *Wt* animals. This is consistent with studies that have identified numerous genes in GBS which facilitate bacterial adhesion to the endothelium, thereby enabling transcytosis and potentially crossing of CNS barriers (*21*, *56*, *57*).

Lineage tracing using *Ms4a3*^{Cre} mice uncovered infection-driven changes in monocyte ontogeny. While GMP-derived monocytes dominate in steady state, infection induced a substantial increase in MDP-derived monocytes, especially in skull marrow and the dura. These populations appear to occupy functionally distinct niches: GMP-derived monocytes exhibit transcriptional programs consistent with classical inflammatory responses, whereas MDP-derived monocytes display features associated with antigen presentation and lymphocyte activation. The persistence of MDP-derived monocytes in the brain and leptomeninges during the resolution phase, together with their enhanced capacity to activate CD4 T cells in vitro, suggests a potential role in coordinating adaptive immune responses following bacterial clearance. Despite this, neither lineage contributed to the long-term maintenance of dural macrophages or microglia, which remained largely dependent on surviving tissue-resident cells. Nevertheless, additional work is needed to understand whether changes in monocyte ontogeny modify disease progression. GMP-Mo express *Mpo* and could contribute to barrier disruption via oxidative stress (*58*). However, increased abundance of GMP-derived monocytes and macrophages has been associated with improved survival in glioblastoma (*59*). Elucidating the signals that govern this ontogenetic shift and its functional consequences will be important for understanding how innate immune diversity shapes CNS infection outcomes.

Furthermore, GBS meningoencephalitis predominantly affects neonates and young infants, whose barrier tissues and immune system undergo rapid changes and differ from adults. These developmental differences likely influence the magnitude, kinetics, and cellular composition of the meningeal immune response. Thus, our model in 6–12 week-old mice may not fully reflect the unique vulnerabilities of the perinatal CNS relevant to neonatal GBS infection. Future studies

applying this infection paradigm to neonatal or early postnatal mice will be important to determine how age-dependent differences in barrier integrity, macrophage maturation, and monocyte ontogeny shape the trajectory of meningeal infection.

In summary, we have integrated fate mapping, microscopy and transcriptomic analysis to highlight a multilayered immune architecture at the CNS border during streptococcal meningoencephalitis. These insights reshape our understanding of myeloid dynamics during bacterial CNS infection, suggesting that monocyte origin, differentiation trajectory, and anatomical context collectively determine their function in disease. Furthermore, the vulnerability of skull marrow progenitors to bacterial invasion and depletion suggests that local hematopoietic niches may influence susceptibility or recovery potential in CNS infections.

MATERIALS AND METHODS

Study design

This study aimed to decipher changes in the myeloid populations in the CNS during streptococcal meningoencephalitis, specifically focusing of microglia, dural macrophages and monocytes. For that purpose, we used a combination of different fate mapping mouse models, as well as microscopy, flow cytometry and transcriptomic analysis. Mice were assigned randomly to experimental groups and were excluded from the study if they didn't show any symptoms of disease after 2 days (including no weight loss and no signs of pain according to mouse grimace scale). To determine group or sample sizes, we have consulted a biostatistician and relied on previous publications. Data are representative of at least two independent experiments unless indicated in the figure legend. Statistical tests are indicated in the respective figure legends.

Mice

Both female and male mice from C57BL/6 genetic background were used at 6 to 12 weeks of age. C57BL/6J and C57BL/6N mice were purchased from Jackson Laboratories (USA) or Charles River Laboratories (Germany) and bred in the local animal facility. CD45.1-mice (B6.SJL-Ptprca Pepcb/BoyJ) were purchased from Jackson Laboratories. Cx3cr1gfp/+ mice were obtained as a kind gift from Steffen Jung (Weizmann Institute, Israel). β-Actin gfp+/− (C57BL/6-Tg(CAG-EGFP)131Osb/LeySopJ) and Ms4a3Cre (C57BL/6J-Ms4a3em2(cre)Fgnx/J) mice were purchased from Jackson Laboratories. Mrc1CreERT2 mice were provided by Marco Prinz (Institute of Neuropathology, Freiburg) as a kind gift. Cxcr4CreERT2 mice were provided by Ralf Stumm (Neuropharmacology, Jena) as a kind gift. Ccr2-/- (B6.129S4-Ccr2tm1Ifc/J) mice were bought from Jackson Laboratories (USA). More details can be found in Supplemental Text.

Mouse interventions

For induction of Cre recombinase by tamoxifen, mice were anesthetized with isoflurane and injected subcutaneously (TAM; 4 mg in 200 µl corn oil; Sigma) at two time points 48 h apart in Cxcr4CreERT2 or Mrc1CreERT2 mice. Control littermates carrying the respective floxed alleles but lacking Cre recombinase were treated identically.

For bone marrow transplantation, recipient mice were anesthetized with ketamine (100 mg/kg) and xylazine (10 mg/kg) administered intraperitoneally. Mice were either head-shielded with a 6 mm lead plate or left unshielded and lethally irradiated (9 Gy), followed by intravenous injection of 5×10^6 donor-derived bone marrow cells. Mice were analyzed 8 weeks after transplantation.

For antibiotic treatment, mice received intraperitoneal injections of ampicillin (100 µg/g body weight) and azithromycin (50 µg/g body weight) in 100 µl sterile water at 2 dpi, followed by administration in drinking water for two weeks (0.4 g/L ampicillin and 0.2 g/L azithromycin). Control mice received PBS injections before antibiotic treatment.

GBS culturing and infection

GBS strain BM110 was used for all infections, kindly provided by Patrick Trieu-Cuot (Institute Pasteur, Paris). Details regarding bacterial growth are described in Supplemental Text. Mice were anesthetized with isoflurane and injected retro-orbitally with 50 µl bacterial suspension (5×10^7 CFU) or PBS vehicle.

CFU assay

Liver, spleen, brain, dura, femoral bone marrow and skull were plated on Granada agar (BD). Detailed description is in Supplemental Text.

Cell extraction

Blood was drawn from the heart. Erythrocytes were lysed in RBC Lysis buffer (eBioscience™ 1X RBC Lysis Buffer). Remaining cells were washed in FACS buffer (PBS + 1% FBS + 2 mM EDTA). Dura mater was peeled from calvaria using forceps and incubated in digestion solution (2.5 mg/ml collagenase IV in RPMI) for 20 min at 37°C shaking, then filtered through 70 µm strainer (BD) and washed with FACS buffer. Calvaria were cleaned of residual muscle and fascia, placed in 1 ml PBS in a 2 ml tube, diced with scissors, filtered through a 70 µm strainer, and washed with FACS buffer. Femurs were cleaned of muscle and bone marrow was flushed with PBS using a 26G needle through a 70 µm strainer. Brains were homogenized and filtered through a 100 µm strainer. Myelin was removed using a 37% Percoll gradient and centrifugation for 30 min at 300 g at room temperature without acceleration or brake.

For bulk RNA-seq samples (dura and brain), tissues were processed identically to avoid potential bias from enzymatic digestion. Briefly, brain and dura were incubated in 2.5 mg/ml collagenase IV for 20 min at 37°C with shaking, filtered through a 70 µm strainer, washed with PBS, resuspended in 37% Percoll, and centrifuged for 30 min at 300 g at room temperature without acceleration or brake. Then, samples were stained as described below.

Flow cytometry and FACS

FcγII/III receptors were blocked by prior 10 min incubation with Fc block (anti mouse CD16/32 antibody Clone 93, Biolegend) on ice. Samples were washed and stained with respective antibodies in FACS buffer for 30 min on ice. Flow cytometry was performed on a 10-color flow cytometer Gallios™ (Beckman Coulter) or Cytoflex S™ (Beckman Coulter) and FACS was done on MofloTM (Beckmann Coulter) or CytoFlex™ (Beckman Coulter). Analysis was done using Kaluza software (v1.5a and 2.1, Beckman Coulter). Further details are in Supplemental Text.

RNA extraction and RT-qPCR

Cells were sorted into RLT lysis buffer (Qiagen) with 1% β-mercaptoethanol. RNA was extracted with RNeasy MicroKit (Qiagen) according to the manufacturer's instructions. RNA was reversely transcribed into cDNA using Superscript IV (Invitrogen). RT-qPCR was performed with absolute qPCR SYBR Green Mix (Thermo Fisher Scientific) using Roche LightcyclerTM 175. mRNA

levels were normalized to *Gapdh* as housekeeping gene. Primer sequences for *Gapdh* were: forward ACTCCACTCACGGCAAATTC; reverse TCTCCATGGTGGTGAAGACA. For *Ccr2*, sequences were: forward ACAGCTCAGGATTAACAGGGACTTG, reverse ACCACTTGCATGCACACATGAC.

Bulk RNA sequencing

For bulk RNA sequencing, described populations were sorted into Rneasy Microkit (Qiagen) lysis buffer containing 1% β-mercaptoethanol. RNA was extracted following manufacturer's protocol. To insure appropriate RNA amounts, samples from two mice were pooled for n=1 in both conditions. Bulk RNA sequencing was performed by CeGat (Tübingen, Germany). Further details are in Supplemental Text.

Single-cell RNA sequencing

For scRNA-seq of myeloid population, dura mater was prepared from five infected and six control Wt mice as described above. Prior to FACS, cells from individual control or infected mice were labelled using the 10X 3' CellPlex Kit Set A (PN-1000261) following manufacturer's recommendations. The $CD45^{+}CD11b^{+}$ cell population was sorted. In total, 5-6 individual animals per group were pooled after FACS. For controls, around 10 750 cells were sorted per mouse (64 500 cells in total), and for infected mice, in average 11 600 cells were sorted per mouse (46 400 cells in total). Sorting was done on separate days for control and infected mice due to technical limitations.

Sorted samples were processed using the 10X Chromium Next GEM Single Cell 3' Kit v3.1 (PN-1000269) and 3´ Feature Barcode Kit (PN-1000262). Single cell droplets were generated using Chromium Next GEM Chip G Single Cell Kit (PN-1000127) and Chromium Controller for 3' gene expression and cell multiplexing libraries were generated according to the manufacturer's specifications. Library quality was assessed using Agilent TapeStation 4150 Cell-free DNA ScreenTape assay (cat. no. 5067-5630) and NEBNext Library Quant Kit for Illumina (cat. no. E7630S). The single cell libraries were sequenced using Ilumina NextSeq1000/2000, with a minimum targeted sequencing depth of 20,000 reads per cell. Fastq files were aligned using the CellRanger version 7.1.

For scRNA-seq of MDP-Mo and GMP-Mo, dura from 4 infected Ms4a3Cre;R26Tomato mice was processed as described above. Prior to FACS, single-cell suspension of each individual mouse was labelled using the 10X 3' CellPlex Kit Set A (PN-1000261) following manufacturer's recommendations. Sorting of MDP-Mo and GMP-Mo was done as described in Fig. S5G. Dump gate included CD206, CD3 and CD19 (all in the APC channel). In total, around 7500 MDP-Mo and 59400 GMP-Mo were sorted. Sorted samples were processed using the 10X Chromium Next GEM Single Cell 3' Kit v3.1 (PN-1000269) and 3´ Feature Barcode Kit (PN-1000262). Single cell droplets were generated using Chromium Next GEM Chip G Single Cell Kit (PN-1000127) and Chromium Controller for 3' gene expression and cell multiplexing libraries were generated according to the manufacturer's specifications. Library quality was assessed using Agilent High Sensitivity DNA Kit (cat. no. 5067-4626). The single cell libraries were sequenced using Ilumina NovaSeq X Plus, with a minimum targeted sequencing depth of 20,000 reads per cell. Fastq files were aligned to prebuilt CellRanger reference refdata-gex-GRCm39-2024-A using the CellRanger version 9.0.1. Downstream analysis can be found in Supplemental Text.

Immunofluorescence labelling

Following transcardial perfusion with ice-cold PBS, brains were fixed in 4% PFA for 24 h and cryoprotected in 30% sucrose at 4°C until sinking. Tissues were embedded in OCT (Sakura, Zoeterwoude, Netherlands) on dry ice and sectioned sagittally (30–40 µm). Sections were permeabilized (0.2% Triton X-100, 2 h), blocked (10% goat serum, 0.1% Triton X-100), and incubated overnight at 4°C with primary antibodies in PBS containing 5% goat serum and 0.05% Triton X-100. After washing (5× PBS), sections were incubated with secondary antibodies and DAPI (1:1000) for 2 h at RT, washed, and mounted using ProLong Diamond (Invitrogen).

Dura whole mounts were prepared as described (17), with minor modifications. After transcardial perfusion with ice-cold PBS, calvaria containing cortical dura mater was placed in 4% PFA overnight at 4°C. The dura was then washed with PBS overnight at 4°C, blocked (5% goat serum, 0.1% Triton X-100, 2 h), and stained overnight at 4°C (2% goat serum, 0.1% Triton X-100, primary antibodies). After washing, samples were incubated with secondary antibodies and DAPI for 2 h at RT, washed, and mounted.

Femur and skull were fixed (4% PFA, overnight), decalcified (Osteosoft®, Sigma Aldrich, for 2 days at 37°C). Then, bones were washed, embedded in OCT, and sectioned (15–20 µm) on gelatin coated slides. Sections were permeabilized (0.2% Triton X-100), blocked (5% goat serum), and stained overnight at 4°C with CD45 (1:100) and anti-GBS (1:200), followed by secondary antibodies and DAPI (2 h, RT). Sections were then washed thoroughly with PBS and mounted using ProLong Diamond Antifade Mountant. Heads were cleared from skin and mandible was removed. Heads were kept in 4% PFA at 4°C overnight, then decalcified (Osteosoft®, Sigma Aldrich, 2 days, 37°C). Heads were then coronally cut with scalpel into approximately 5 mm slices and frozen in OCT compound. 70-80 cryosections were mounted on gelatin-coated slides. The downstream processing and staining were the same as for the brain. All antibodies and dilutions used are in Supplemental Text.

Confocal microscopy

Confocal microscopy was performed with LSM 880 or LSM 980 confocal microscopes equipped with Plan-Apochromat objectives (10×/0.3, 20×/0.8 NA, and 40×/1.2, Carl Zeiss Microimaging) using 1-1.5 µm optical slices, at RT. Images are displayed as maximum-intensity projections of 10-20 µm thick (for skull and femur) or 30-40µm thick z stacks (for brain and dura), 1024x1024 pixel resolution. Sample localization was performed using the AI Sample Finder function (Zeiss LSM 980). No autofocus was used. Excitation was performed using appropriate laser lines (e.g., 405 nm for DAPI, 488 nm for AF488, GFP, 561 nm for PE, Tomato, and 633 nm for AF633).

Image analysis

Maximum-intensity projections were generated from z-stacks using ZEN 3.0SR (Black, Zeiss). Area and fluorescence intensity were measured using ZEN 3.0 (Blue edition, Zeiss). For enumeration of dural macrophages per field of view, the pictures were taken on approximately same locations in each dura. CX3CR1-GFP+ dural macrophages were manually counted using ImageJ (version 1.54p) Cell counter. No deconvolution or nonlinear image processing was applied. Only linear adjustments of brightness and contrast were performed uniformly across entire images.

Statistical analysis

GraphPad Prism (version 10.0.0; GraphPad Prism) was used for all statistical analyses.

Comparisons between two populations isolated from the same mice were performed using a two-tailed paired t-test. For comparisons between two independent groups, either an unpaired two-tailed Student's t-test or a Mann–Whitney U test was applied, unless stated otherwise. For multiple pairwise comparisons within a single dataset, Holm–Šídák correction was used. For experiments involving multiple groups, one-way or two-way ANOVA was performed, followed by Tukey's or Šídák's post hoc multiple-comparison tests, with adjusted p-values reported. The analysis used for each experiment can be found in figure legends, with the number of replicates and independent experiments and in Data file S2. Differences were considered statistically significant if p-values were < 0.05. (ns, not significant; *$p < 0.05$; **$p < 0.01$;***$p < 0.001$; ****$p < 0.0001$). Data are represented as mean ± SEM if not stated otherwise.

List of supplementary materials:

Supplementary Methods

Supplemental figures 1-7

Data file S1. Complete list of GO Terms from MDP-Mo and GMP-Mo GO Terms for biological processes, with exclusions of the genes overlapping with GSE262369.

Data file S2. Raw data file

Reproducibility checklist

References

1. J. Kolter, P. Henneke, Codevelopment of Microbiota and Innate Immunity and the Risk for Group B Streptococcal Disease. *Front. Immunol.* **8**, 1497 (2017).

2. M. Kohli-Lynch, N. J. Russell, A. C. Seale, Z. Dangor, C. J. Tann, C. J. Baker, L. Bartlett, C. Cutland, M. G. Gravett, P. T. Heath, M. Ip, K. Le Doare, S. A. Madhi, C. E. Rubens, S. K. Saha, S. Schrag, A. Sobanjo-ter Meulen, J. Vekemans, C. O'Sullivan, F. Nakwa, H. Ben Hamouda, H. Soua, K. Giorgakoudi, S. Ladhani, T. Lamagni, H. Rattue, C. Trotter, J. E. Lawn, Neurodevelopmental Impairment in Children After Group B Streptococcal Disease Worldwide: Systematic Review and Meta-analyses. *Clinical Infectious Diseases* **65**, S190–S199 (2017).

3. A. C. Seale, F. Bianchi-Jassir, N. J. Russell, M. Kohli-Lynch, C. J. Tann, J. Hall, L. Madrid, H. Blencowe, S. Cousens, C. J. Baker, L. Bartlett, C. Cutland, M. G. Gravett, P. T. Heath, M. Ip, K. Le Doare, S. A. Madhi, C. E. Rubens, S. K. Saha, S. J. Schrag, A. Sobanjo-ter Meulen, J. Vekemans, J. E. Lawn, Estimates of the Burden of Group B Streptococcal Disease Worldwide for Pregnant Women, Stillbirths, and Children. *Clinical Infectious Diseases* **65**, S200–S219 (2017).

4. R. Rua, J. Y. Lee, A. B. Silva, I. S. Swafford, D. Maric, K. R. Johnson, D. B. McGavern, Infection drives meningeal engraftment by inflammatory monocytes that impairs CNS immunity. *Nat Immunol* **20**, 407–419 (2019).

5. J. Rebejac, E. Eme-Scolan, L. Arnaud Paroutaud, S. Kharbouche, M. Teleman, L. Spinelli, E. Gallo, A. Roussel-Queval, A. Zarubica, A. Sansoni, Q. Bardin, P. Hoest, M.-C. Michallet, C. Brousse, K. Crozat, M. Manglani, Z. Liu, F. Ginhoux, D. B. McGavern, M. Dalod, B. Malissen, T. Lawrence, R. Rua, Meningeal macrophages protect against viral neuroinfection. *Immunity* **55**, 2103-2117.e10 (2022).

6. V. Gres, J. Kolter, D. Erny, P. Henneke, The role of CNS macrophages in streptococcal meningoencephalitis. *Journal of Leukocyte Biology* **106**, 209–218 (2019).

7. M. Prinz, D. Erny, N. Hagemeyer, Ontogeny and homeostasis of CNS myeloid cells. *Nat Immunol* **18**, 385–392 (2017).

8. K. Alves De Lima, J. Rustenhoven, J. Kipnis, Meningeal Immunity and Its Function in Maintenance of the Central Nervous System in Health and Disease. *Annu. Rev. Immunol.* **38**, 597–620 (2020).

9. H. Van Hove, L. Martens, I. Scheyltjens, K. De Vlaminck, A. R. Pombo Antunes, S. De Prijck, N. Vandamme, S. De Schepper, G. Van Isterdael, C. L. Scott, J. Aerts, G. Berx, G. E. Boeckxstaens, R. E. Vandenbroucke, L. Vereecke, D. Moechars, M. Guilliams, J. A. Van Ginderachter, Y. Saeys, K. Movahedi, A single-cell atlas of mouse brain macrophages reveals unique transcriptional identities shaped by ontogeny and tissue environment. *Nat Neurosci* **22**, 1021–1035 (2019).

10. J. Rustenhoven, A. Drieu, T. Mamuladze, K. A. De Lima, T. Dykstra, M. Wall, Z. Papadopoulos, M. Kanamori, A. F. Salvador, W. Baker, M. Lemieux, S. Da Mesquita, A. Cugurra, J. Fitzpatrick, S. Sviben, R. Kossina, P. Bayguinov, R. R. Townsend, Q. Zhang, P. Erdmann-Gilmore, I. Smirnov, M.-B. Lopes, J. Herz, J. Kipnis, Functional

characterization of the dural sinuses as a neuroimmune interface. *Cell* **184**, 1000-1016.e27 (2021).

11. J. A. Mazzitelli, L. C. D. Smyth, K. A. Cross, T. Dykstra, J. Sun, S. Du, T. Mamuladze, I. Smirnov, J. Rustenhoven, J. Kipnis, Cerebrospinal fluid regulates skull bone marrow niches via direct access through dural channels. *Nat Neurosci* **25**, 555–560 (2022).

12. A. Cugurra, T. Mamuladze, J. Rustenhoven, T. Dykstra, G. Beroshvili, Z. J. Greenberg, W. Baker, Z. Papadopoulos, A. Drieu, S. Blackburn, M. Kanamori, S. Brioschi, J. Herz, L. G. Schuettpelz, M. Colonna, I. Smirnov, J. Kipnis, Skull and vertebral bone marrow are myeloid cell reservoirs for the meninges and CNS parenchyma. *Science* **373**, eabf7844 (2021).

13. F. E. Pulous, J. C. Cruz-Hernández, C. Yang, Z. Kaya, A. Paccalet, G. Wojtkiewicz, D. Capen, D. Brown, J. W. Wu, M. J. Schloss, C. Vinegoni, D. Richter, M. Yamazoe, M. Hulsmans, N. Momin, J. Grune, D. Rohde, C. S. McAlpine, P. Panizzi, R. Weissleder, D.-E. Kim, F. K. Swirski, C. P. Lin, M. A. Moskowitz, M. Nahrendorf, Cerebrospinal fluid can exit into the skull bone marrow and instruct cranial hematopoiesis in mice with bacterial meningitis. *Nat Neurosci* **25**, 567–576 (2022).

14. B. Ajami, J. L. Bennett, C. Krieger, K. M. McNagny, F. M. V. Rossi, Infiltrating monocytes trigger EAE progression, but do not contribute to the resident microglia pool. *Nat Neurosci* **14**, 1142–1149 (2011).

15. R. M. Ritzel, A. R. Patel, J. M. Grenier, J. Crapser, R. Verma, E. R. Jellison, L. D. McCullough, Functional differences between microglia and monocytes after ischemic stroke. *J Neuroinflammation* **12**, 1–12 (2015).

16. S. Lehnardt, P. Henneke, E. Lien, D. L. Kasper, J. J. Volpe, I. Bechmann, R. Nitsch, J. R. Weber, D. T. Golenbock, T. Vartanian, A Mechanism for Neurodegeneration Induced by Group B Streptococci through Activation of the TLR2/MyD88 Pathway in Microglia. *J Immunol* **177**, 583–592 (2006).

17. F. A. Pinho-Ribeiro, L. Deng, D. V. Neel, O. Erdogan, H. Basu, D. Yang, S. Choi, A. J. Walker, S. Carneiro-Nascimento, K. He, G. Wu, B. Stevens, K. S. Doran, D. Levy, I. M. Chiu, Bacteria hijack a meningeal neuroimmune axis to facilitate brain invasion. *Nature* **615**, 472–481 (2023).

18. M. Djukic, Circulating monocytes engraft in the brain, differentiate into microglia and contribute to the pathology following meningitis in mice. *Brain* **129**, 2394–2403 (2006).

19. M. M. Koopmans, J. Engelen-Lee, M. C. Brouwer, V. Jaspers, W. K. Man, M. V. Seron, D. van de Beek, Characterization of a Listeria monocytogenes meningitis mouse model. *Journal of Neuroinflammation* **15** (2018).

20. M. N. van Kassel, G. de Boer, S. A. F. Teeri, D. Jamrozy, S. D. Bentley, M. C. Brouwer, A. van der Ende, D. van de Beek, M. W. Bijlsma, Molecular epidemiology and mortality of group B streptococcal meningitis and infant sepsis in the Netherlands: a 30-year nationwide surveillance study. *The Lancet Microbe* **2**, e32–e40 (2021).

21. A. Tazi, S. Bellais, I. Tardieux, S. Dramsi, P. Trieu-Cuot, C. Poyart, Group B Streptococcus surface proteins as major determinants for meningeal tropism. *Current Opinion in Microbiology* **15**, 44–49 (2012).

22. B. Périchon, N. Szili, L. Du Merle, I. Rosinski-Chupin, M. Gominet, S. Bellais, C. Poyart, P. Trieu-Cuot, S. Dramsi, Regulation of PI-2b Pilus Expression in Hypervirulent Streptococcus agalactiae ST-17 BM110. *PLoS ONE* **12**, e0169840 (2017).

23. G. Mancuso, A. Midiri, C. Beninati, C. Biondo, R. Galbo, S. Akira, P. Henneke, D. Golenbock, G. Teti, Dual Role of TLR2 and Myeloid Differentiation Factor 88 in a Mouse Model of Invasive Group B Streptococcal Disease. *J Immunol* **172**, 6324–6329 (2004).

24. R. Feuerstein, V. Gres, N. Elias Perdigó, S. Baasch, M. Freudenhammer, R. Elling, P. Henneke, Macrophages Are a Potent Source of Streptococcus-Induced IFN-β. *J Immunol* **203**, 3416–3426 (2019).

25. M. K. Sharief, M. Ciardi, E. J. Thompson, Blood-Brain Barrier Damage in Patients with Bacterial Meningitis: Association with Tumor Necrosis Factor- but not Interleukin-I. *Journal of Infectious Diseases* **166**, 350–358 (1992).

26. J. C. Cronk, A. J. Filiano, A. Louveau, I. Marin, R. Marsh, E. Ji, D. H. Goldman, I. Smirnov, N. Geraci, S. Acton, C. C. Overall, J. Kipnis, Peripherally derived macrophages can engraft the brain independent of irradiation and maintain an identity distinct from microglia. *Journal of Experimental Medicine* **215**, 1627–1647 (2018).

27. F. C. Bennett, M. L. Bennett, F. Yaqoob, S. B. Mulinyawe, G. A. Grant, M. Hayden Gephart, E. D. Plowey, B. A. Barres, A Combination of Ontogeny and CNS Environment Establishes Microglial Identity. *Neuron* **98**, 1170-1183.e8 (2018).

28. Y. Werner, E. Mass, P. Ashok Kumar, T. Ulas, K. Händler, A. Horne, K. Klee, A. Lupp, D. Schütz, F. Saaber, C. Redecker, J. L. Schultze, F. Geissmann, R. Stumm, Cxcr4 distinguishes HSC-derived monocytes from microglia and reveals monocyte immune responses to experimental stroke. *Nat Neurosci* **23**, 351–362 (2020).

29. Y. Huang, Z. Xu, S. Xiong, F. Sun, G. Qin, G. Hu, J. Wang, L. Zhao, Y.-X. Liang, T. Wu, Z. Lu, M. S. Humayun, K.-F. So, Y. Pan, N. Li, T.-F. Yuan, Y. Rao, B. Peng, Repopulated microglia are solely derived from the proliferation of residual microglia after acute depletion. *Nat Neurosci* **21**, 530–540 (2018).

30. T. Goldmann, P. Wieghofer, M. J. C. Jordão, F. Prutek, N. Hagemeyer, K. Frenzel, L. Amann, O. Staszewski, K. Kierdorf, M. Krueger, G. Locatelli, H. Hochgerner, R. Zeiser, S. Epelman, F. Geissmann, J. Priller, F. M. V. Rossi, I. Bechmann, M. Kerschensteiner, S. Linnarsson, S. Jung, M. Prinz, Origin, fate and dynamics of macrophages at central nervous system interfaces. *Nat Immunol* **17**, 797–805 (2016).

31. C. Blériot, T. Dupuis, G. Jouvion, G. Eberl, O. Disson, M. Lecuit, Liver-Resident Macrophage Necroptosis Orchestrates Type 1 Microbicidal Inflammation and Type-2-Mediated Tissue Repair during Bacterial Infection. *Immunity* **42**, 145–158 (2015).

32. N. Robinson, S. McComb, R. Mulligan, R. Dudani, L. Krishnan, S. Sad, Type I interferon induces necroptosis in macrophages during infection with Salmonella enterica serovar Typhimurium. *Nat Immunol* **13**, 954–962 (2012).

33. N. V. Serbina, E. G. Pamer, Monocyte emigration from bone marrow during bacterial infection requires signals mediated by chemokine receptor CCR2. *Nat Immunol* **7**, 311–317 (2006).

34. S. Brioschi, W.-L. Wang, V. Peng, M. Wang, I. Shchukina, Z. J. Greenberg, J. K. Bando, N. Jaeger, R. S. Czepielewski, A. Swain, D. A. Mogilenko, W. L. Beatty, P. Bayguinov, J. A. J. Fitzpatrick, L. G. Schuettpelz, C. C. Fronick, I. Smirnov, J. Kipnis, V. S. Shapiro, G. F. Wu, S. Gilfillan, M. Cella, M. N. Artyomov, S. H. Kleinstein, M. Colonna, Heterogeneity of meningeal B cells reveals a lymphopoietic niche at the CNS borders. *Science*, doi: 10.1126/science.abf9277 (2021).

35. A. Mildner, H. Schmidt, M. Nitsche, D. Merkler, U.-K. Hanisch, M. Mack, M. Heikenwalder, W. Brück, J. Priller, M. Prinz, Microglia in the adult brain arise from Ly-6ChiCCR2+ monocytes only under defined host conditions. *Nat Neurosci* **10**, 1544–1553 (2007).

36. F. Geissmann, S. Jung, D. R. Littman, Blood Monocytes Consist of Two Principal Subsets with Distinct Migratory Properties. *Immunity* **19**, 71–82 (2003).

37. J. W. Swann, O. C. Olson, E. Passegué, Made to order: emergency myelopoiesis and demand-adapted innate immune cell production. *Nat Rev Immunol* **24**, 596–613 (2024).

38. A. Yáñez, S. G. Coetzee, A. Olsson, D. E. Muench, B. P. Berman, D. J. Hazelett, N. Salomonis, H. L. Grimes, H. S. Goodridge, Granulocyte-Monocyte Progenitors and Monocyte-Dendritic Cell Progenitors Independently Produce Functionally Distinct Monocytes. *Immunity* **47**, 890-902.e4 (2017).

39. Z. Liu, Y. Gu, S. Chakarov, C. Bleriot, I. Kwok, X. Chen, A. Shin, W. Huang, R. J. Dress, C.-A. Dutertre, A. Schlitzer, J. Chen, L. G. Ng, H. Wang, Z. Liu, B. Su, F. Ginhoux, Fate Mapping via Ms4a3-Expression History Traces Monocyte-Derived Cells. *Cell* **178**, 1509-1525.e19 (2019).

40. S. Trzebanski, J.-S. Kim, N. Larossi, A. Raanan, D. Kancheva, J. Bastos, M. Haddad, A. Solomon, E. Sivan, D. Aizik, J. S. Kralova, M. Gross-Vered, S. Boura-Halfon, T. Lapidot, R. Alon, K. Movahedi, S. Jung, Classical monocyte ontogeny dictates their functions and fates as tissue macrophages. *Immunity*, S1074-7613(24)00224–3 (2024).

41. A. Aspelund, S. Antila, S. T. Proulx, T. V. Karlsen, S. Karaman, M. Detmar, H. Wiig, K. Alitalo, A dural lymphatic vascular system that drains brain interstitial fluid and macromolecules. *Journal of Experimental Medicine* **212**, 991–999 (2015).

42. L. M. Harden, S. Leahy, S. G. Lala, P. Paul, J. Chandna, S. Lowick, S. Mbatha, T. Jaye, B. Laughton, A. Ghoor, P. Sithole, J. Msayi, N. Kumalo, T. N. Msibi, S. A. Madhi, J. E. Lawn, Z. Dangor, South African Children: A Matched Cohort Study of Neurodevelopmental Impairment in Survivors of Invasive Group B *Streptococcus* Disease Aged 5 to 8 Years. *Clinical Infectious Diseases* **74**, S5–S13 (2022).

43. J. V. Forrester, P. G. McMenamin, S. J. Dando, CNS infection and immune privilege. *Nat Rev Neurosci* **19**, 655–671 (2018).

44. J. S. Braun, J. E. Sublett, D. Freyer, T. J. Mitchell, J. L. Cleveland, E. I. Tuomanen, J. R. Weber, Pneumococcal pneumolysin and H_2O_2 mediate brain cell apoptosis during meningitis. *J Clin Invest* **109**, 19–27 (2002).

45. J. Zweigner, S. Jackowski, S. H. Smith, M. van der Merwe, J. R. Weber, E. I. Tuomanen, Bacterial Inhibition of Phosphatidylcholine Synthesis Triggers Apoptosis in the Brain. *J Exp Med* **200**, 99–106 (2004).

46. A. J. Schain, A. Melo-Carrillo, D. Borsook, J. Grutzendler, A. M. Strassman, R. Burstein, Activation of pial and dural macrophages and dendritic cells by cortical spreading depression. *Annals of Neurology* **83**, 508–521 (2018).

47. F. Herisson, V. Frodermann, G. Courties, D. Rohde, Y. Sun, K. Vandoorne, G. R. Wojtkiewicz, G. S. Masson, C. Vinegoni, J. Kim, D.-E. Kim, R. Weissleder, F. K. Swirski, M. A. Moskowitz, M. Nahrendorf, Direct vascular channels connect skull bone marrow and the brain surface enabling myeloid cell migration. *Nat Neurosci* **21**, 1209–1217 (2018).

48. Z. I. Kolabas, L. B. Kuemmerle, R. Perneczky, B. Förstera, S. Ulukaya, M. Ali, S. Kapoor, L. M. Bartos, M. Büttner, O. S. Caliskan, Z. Rong, H. Mai, L. Höher, D. Jeridi, M. Molbay, I. Khalin, I. K. Deligiannis, M. Negwer, K. Roberts, A. Simats, O. Carofiglio, M. I. Todorov, I. Horvath, F. Ozturk, S. Hummel, G. Biechele, A. Zatcepin, M. Unterrainer, J. Gnörich, J. Roodselaar, J. Shrouder, P. Khosravani, B. Tast, L. Richter, L. Díaz-Marugán, D. Kaltenecker, L. Lux, Y. Chen, S. Zhao, B.-S. Rauchmann, M. Sterr, I. Kunze, K. Stanic, V. W. Y. Kan, S. Besson-Girard, S. Katzdobler, C. Palleis, J. Schädler, J. C. Paetzold, S. Liebscher, A. E. Hauser, O. Gokce, H. Lickert, H. Steinke, C. Benakis, C. Braun, C. P. Martinez-Jimenez, K. Buerger, N. L. Albert, G. Höglinger, J. Levin, C. Haass, A. Kopczak, M. Dichgans, J. Havla, T. Kümpfel, M. Kerschensteiner, M. Schifferer, M. Simons, A. Liesz, N. Krahmer, O. A. Bayraktar, N. Franzmeier, N. Plesnila, S. Erener, V. G. Puelles, C. Delbridge, H. S. Bhatia, F. Hellal, M. Elsner, I. Bechmann, B. Ondruschka, M. Brendel, F. J. Theis, A. Erturk, Distinct molecular profiles of skull bone marrow in health and neurological disorders. *Cell* **186**, 3706-3725.e29 (2023).

49. Z. Fitzpatrick, N. G. Zanluqui, J. S. Rosenblum, Z. K. Tuong, C. Y. C. Lee, V. Chandrashekhar, M. L. Negro-Demontel, A. P. Stewart, D. A. Posner, M. Buckley, K. S. J. Allinson, P. Mastorakos, P. Chittiboina, D. Maric, D. Donahue, A. Helmy, T. Tajsic, J. R. Ferdinand, A. Portet, A. Peñalver, E. Gillman, Z. Zhuang, M. R. Clatworthy, D. B. McGavern, Venous-plexus-associated lymphoid hubs support meningeal humoral immunity. *Nature* **628**, 612–619 (2024).

50. L. Amann, A. Fell, G. Monaco, R. Sankowski, H. Z. Q. Wu, M. J. C. Jordão, K. Borst, M. Fliegauf, T. Masuda, A. Ardura-Fabregat, N. Paterson, E. Nent, J. Cook, O. Staszewski, O. Mossad, T. Falk, A. Louveau, I. Smirnov, J. Kipnis, T. Lämmermann, M. Prinz, Extrasinusoidal macrophages are a distinct subset of immunologically active dural macrophages. *Science Immunology*, doi: 10.1126/sciimmunol.adh1129 (2024).

51. M. W. Barth, J. A. Hendrzak, M. J. Melnicoff, P. S. Morahan, Review of the macrophage disappearance reaction. *Journal of Leukocyte Biology* **57**, 361–367 (1995).

52. P. A. Louwe, L. Badiola Gomez, H. Webster, G. Perona-Wright, C. C. Bain, S. J. Forbes, S. J. Jenkins, Recruited macrophages that colonize the post-inflammatory peritoneal niche convert into functionally divergent resident cells. *Nat Commun* **12**, 1–15 (2021).

53. S. M. Lai, J. Sheng, P. Gupta, L. Renia, K. Duan, F. Zolezzi, K. Karjalainen, E. W. Newell, C. Ruedl, Organ-Specific Fate, Recruitment, and Refilling Dynamics of Tissue-Resident Macrophages during Blood-Stage Malaria. *Cell Reports* **25**, 3099-3109.e3 (2018).

54. M. Filaferro, C. Novi, V. Ruggieri, S. Genedani, S. Alboni, D. Malagoli, G. Caló, R. Guerrini, G. Vitale, Neuropeptide S stimulates human monocyte chemotaxis via NPS receptor activation. *Peptides* **39**, 16–20 (2013).

55. F. Tacke, D. Alvarez, T. J. Kaplan, C. Jakubzick, R. Spanbroek, J. Llodra, A. Garin, J. Liu, M. Mack, N. van Rooijen, S. A. Lira, A. J. Habenicht, G. J. Randolph, Monocyte subsets differentially employ CCR2, CCR5, and CX3CR1 to accumulate within atherosclerotic plaques. *J Clin Invest* **117**, 185–194 (2007).

56. B. J. Kim, M. A. McDonagh, L. Deng, B. D. Gastfriend, A. Schubert-Unkmeir, K. S. Doran, E. V. Shusta, Streptococcus agalactiae disrupts P-glycoprotein function in brain endothelial cells. *Fluids Barriers CNS* **16**, 26 (2019).

57. K. S. Doran, E. J. Engelson, A. Khosravi, H. C. Maisey, I. Fedtke, O. Equils, K. S. Michelsen, M. Arditi, A. Peschel, V. Nizet, Blood-brain barrier invasion by group B *Streptococcus* depends upon proper cell-surface anchoring of lipoteichoic acid. *J Clin Invest* **115**, 2499–2507 (2005).

58. T. Barichello, J. S. Generoso, L. R. Simões, S. G. Elias, J. Quevedo, Role of Oxidative Stress in the Pathophysiology of Pneumococcal Meningitis. *Oxidative Medicine and Cellular Longevity* **2013**, 371465 (2013).

59. E. Karimi, M. W. Yu, S. M. Maritan, L. J. M. Perus, M. Rezanejad, M. Sorin, M. Dankner, P. Fallah, S. Doré, D. Zuo, B. Fiset, D. J. Kloosterman, L. Ramsay, Y. Wei, S. Lam, R. Alsajjan, I. R. Watson, G. Roldan Urgoiti, M. Park, D. Brandsma, D. L. Senger, J. A. Chan, L. Akkari, K. Petrecca, M.-C. Guiot, P. M. Siegel, D. F. Quail, L. A. Walsh, Single-cell spatial immune landscapes of primary and metastatic brain tumours. *Nature* **614**, 555–563 (2023).

60. L. Kolberg, U. Raudvere, I. Kuzmin, P. Adler, J. Vilo, H. Peterson, g:Profiler—interoperable web service for functional enrichment analysis and gene identifier mapping (2023 update). *Nucleic Acids Research* **51**, W207–W212 (2023).

61. Morpheus. https://software.broadinstitute.org/morpheus/.

Acknowledgments: We thank Anita Imm, Reem Alsumati, Adriana Greco and Lena Grubišić for their great technical assistance. We thank the ZTZ core facility, especially Jan Bodinek, Marie Follo and Franck-Anicet Ditengou for their great technical assistance. We thank the Center for Experimental Models and Transgenic Service (CEMT) of University Medical Center

Freiburg for excellent technical support and assistance with the animal studies performed in this work. We thank Pedro Aniceto for his assistance with analysis in R and R Studio.

Funding: AL and FL were supported by the IMM-PACT clinician scientist programme, funded by the Deutsche Forschungsgesellschaft (DFG, German Research Foundation) – 413517907. PH, MP, KK, JK, S, JK and DE received funding the via TRR359 (DFG, project ID 491676693); MP, SJ, KK, AL, DE and PH received funding via TRR167 (project ID 259373024); MP, KK and PH were funded via CRC1160 (DFG, project ID 256073931). PH received further support from the DFG (HE3127/9, HE3127/12, HE3127/16). DE was further supported by the Berta-Ottenstein-Programme for advanced Clinician Scientists, the Else Kröner-Fresenius-Stiftung and Ministry of Science, Research and Arts, Baden-Wuerttemberg under the aegis of JPND. This study was supported in part by the Excellence Initiative of the German Research Foundation (GSC-4, Spemann Graduate School) and in part by the Ministry for Science, Research and Arts of the State of Baden-Württemberg.

Author contributions: Conceptualization: PH, VG. Supervision: PH, DE. Formal analysis: VG, FL, LFPB, GM, S, DO. Investigation: VG, VF, AL, JN, ZMM, TM, SB, JH. Resources: PH, KPK, MP, SJ. Validation: VG, JK. Visualization: VG. Writing – original draft: VG, PH. Writing – review and editing: PH, KK, JK, DE, S, FL, AL, JK, SB, VF, JN, ZMM.

Competing interests: All authors declare that they have no competing interests.

Data, code and materials availability: Transcriptome data generated in this study have been deposited in GEO under the accession numbers GSE269731, GSE269398 and GSE316230. Tabulated data underlying the figures is provided in data file S2. All other data needed to support the conclusions of the paper are present in the paper or the Supplementary Materials. No custom code was generated. All materials are commercially available as described in the Materials and Methods.

FIGURE CAPTIONS

Fig. 1: The meninges serve as a reactive CNS barrier during hematogenous Group B streptococcal (GBS) infection A: Wt mice were injected i.v. with 5×10^7 CFU GBS. CFU counts at 2 dpi in homogenized brain (n=25), dura (n=21), liver (n=16), femur bone marrow (n=19), skull (n=25), and blood (CFU/ml, n=24) from 5-8 independent experiments. **B-C:** Sagittal brain sections from infected (inf) *Cx3cr1*$^{gfp/+}$ mice showing leptomeninges (LpM) and parenchyma (**B**) or choroid plexus (ChP) (**C**). Arrows indicate GBS in parenchyma and ChP. Scale bar=50 µm. **D:** Quantification of GBS signal normalized to area in leptomeninges (LpM), cortical parenchyma, and ChP (lateral or third ventricle). One-way ANOVA with Tukey's multiple comparisons correction; n=7 from 4 experiments. **E:** Dural whole mount from infected *Cx3cr1*$^{gfp/+}$ mice, sinus and extra-sinus regions. Scale bar=20 µm. **F:** Microglia (MG), monocytes (Mo), neutrophils (Neu) and CNS-associated macrophage (CAM) numbers, from control (Ctrl) and infected (Inf) brains, by flow cytometry. n=5-7, from 3 experiments. Multiple Mann-Whitney test, Holm-Šídák correction. **G**: Correlation between brain CFU and Mo or Neu numbers (Spearman); linear regression. n=20 from 6 experiments; R=goodness of fit. **H:** Mo, Neu and dural macrophage (DM) numbers from control and infected dura, by flow cytometry, n=7 from 3 experiments. Multiple Mann–Whitney, Holm–Šídák correction. **I:** Dural whole mounts from control and infected *Cx3cr1*$^{gfp/+}$ mice, showing loss of GFP$^+$ dural macrophages in sinus and extra-sinus regions. Scale bar=50 µm. **J:** *Cx3cr1*$^{gfp/+}$ dural macrophages per field of view (FOV) in sinus and extra-sinus dura. 2-3 positions per mouse were averaged. n=3-4, from 2 experiments. Two-way ANOVA with Šídák's multiple comparisons test. **K:** Coronal head section from infected *Ms4a3*^{Cre}*;R26*^{Tomato} mouse. Scale bar=100 µm. **L:** *Mrc1*^{CreERT2}*;R26*^{Tomato} mice received tamoxifen (TAM) twice 8 weeks before infection. At 2 dpi, dural macrophages and microglia were sorted from dura and brain. Two mice were pooled per sample (n=3; 6 mice). **M:** Principal component analysis (PCA) of bulk RNA-seq from sorted populations. **N:** Z-score heat map of 93 genes upregulated in both microglia and dural macrophages ($log_2FC > 1.5$, padj<0.05). **O:** Scatter plot comparing log_2FC of genes upregulated in microglia and dural macrophages.

Fig. 2: Loss of dural macrophages triggers compensatory monocyte differentiation

A: Experimental timeline. *Cxcr4*$^{CreERT2;}$*R26*^{Tomato} mice received TAM 8 weeks before GBS infection and analyzed at 2 dpi. **B:** Percentage of Tomato$^+$ dural macrophages (DM) (CD45^{hi}CD11b$^+$Ly6C^{neg}Ly6G^{neg}CD206$^+$) and Tomato^{neg} microglia (MG) (CD45^{lo}CD11b$^+$Ly6C^{neg}Ly6G^{neg}CD206^{neg}). Mann-Whitney U-test; n=4-5 from 3 independent experiments. **C:** Representative flow cytometry plots showing Ly6C^{hi}CD206$^+$ population in Ctrl and Inf dura. Numbers indicate percentages. **D:** Quantification of Ly6C^{hi}CD206$^+$ population in Ctrl and Inf mice, n=7 from 3 experiments. Mann-Whitney U-test. **E:** Percentage of Tomato-labeling in *Cxcr4*$^{CreERT2;}$*R26*^{Tom} mice in Ly6C^{hi}CD206$^+$ population in comparison to Ly6C^{hi}CD206^{neg} monocytes and Ly6C^{neg}CD206$^+$ macrophages in infected dura. n=4, from 2 experiments. One-way ANOVA with Tukey's multiple comparisons. **F:** MHC-II expression (MFI) in Ly6C^{hi}CD206$^+$ population compared with Ly6C^{hi}CD206^{neg} monocytes and Ly6C^{neg}CD206$^+$ dural macrophages. n=8, from 3 experiments. One-way ANOVA with Tukey's test. **G:** Experimental timeline for sorting of myeloid population for single-cell RNA sequencing. **H:** UMAP representation of gene expression profiles of sorted CD45$^+$CD11b$^+$ myeloid population from control and infected dura of *Wt* mice. n (mice)=6 for Ctrl condition, n(mice)=5 for Inf condition, from one experiment per condition. Cell numbers per condition are underlined. **I-J:**

Relative abundance of dural macrophages (0, 2, 3, 4), neutrophil and monocyte (1, 5, 6, 7) clusters expressed as percentages of total myeloid cells according to brain bacterial burden or control levels. Colors correspond to clusters in **H**. **K**: Linear regression of *Mrc1*, *H2-Ab1* and *Cd74* expression in infection-associated monocytes (cluster 5) versus brain GBS CFU counts. Pearson correlation used to calculate R. **L:** Adoptive transfer scheme. *Wt* mice were infected and received 1.2-4x10^5 monocyte progenitors (MP) from *β-Actin-GFP* bone marrow at 1 dpi. Controls received PBS before adoptive transfer. **M:** Flow cytometry showing partial CD206 upregulation in *β-Actin-GFP* monocyte progenitors after transfer. **N:** Representative image of infected dura showing a donor-derived GFP^+ progenitor upregulating CD206 (arrow). Scale bar=20 µm.

Fig. 3: Distinct monocyte sources support dural immunity in steady state and infection

A: Flow cytometry analysis of dural monocytes (Mo) in control and infected *Wt* or *Ccr2*$^{-/-}$ mice. n=7-10, from 4 experiments. Two-way ANOVA with Tukey's test. **B:** Monocyte frequencies in brains of control and infected Wt or $Ccr2^{-/-}$ mice measured by flow cytometry. n=4–6 from 3 experiments. Two-way ANOVA with Tukey's test. **C:** Experimental scheme for irradiation and bone marrow transplantation; analysis performed 8 weeks later. **D:** Flow cytometry depicting donor-originating GFP^+ monocytes. Numbers indicate percentages within gated GFP^+ monocytes. **E:** Relative chimerism of dural monocytes compared with skull or femur bone marrow monocytes. Two-way ANOVA with Šídák's correction; n=7-8 from 4 experiments. **F:** Representative flow cytometry plots depicting donor-originating GFP^+ dural macrophages (DM). Percentages shown in the gate. **G:** Chimerism of dural macrophages in fully irradiated versus head-shielded mice. Mann-Whitney U – test. n=7-8, from 4 independent experiments. **H:** Experimental timeline for head-shielded chimeras. Eight weeks after irradiation and bone marrow transfer, mice were infected with GBS and analyzed at 2 dpi. **I:** Relative chimerism of dural monocytes compared with skull or femur monocytes in control and infected head-shielded mice. n=6–8 from 4 experiments. Two-way ANOVA with Šídák's correction. **J:** Quantification of GFP fluorescence intensity normalized to dura area in whole mounts (representative images in Fig. S3I). n=3, one-way ANOVA with Tukey's test, from 2 experiments. **K:** Representative microscopy of femur or skull bone marrow or whole mount dura following transplantation from *Cx3cr1*$^{gfp/+}$ donors in fully irradiated or head-shielded mice, included infected head-shielded mice. Scale bar=50 µm. **L:** Dural macrophage chimerism after infection measured by flow cytometry. Unpaired t-test; n=6–8 from 4 experiments. **M:** Femur and skull marrow from infected *Ms4a3*^{Cre}*;R26*^{Tomato} mice stained for GBS-AF633 (yellow). Scale bar(left)=20 µm, (right)=5 µm. **N–R:** Absolute numbers of CMP (N), GMP (O), MDP (P), monocyte progenitors including cMoP and iMoP (Q), and monocytes (R) in femur and skull marrow in steady state and infection. Multiple unpaired t-tests with Holm–Šídák correction; n=4–7 from 2-3 experiments.

Fig. 4: GBS infection reprograms monocyte ontogeny toward MDP-derived lineages

A: Scheme of either GMP or MDP-derived monocyte lineages and respective mouse models used to either label GMP-derived cells (*Ms4a3*^{Cre}*;R26*^{Tomato}) or all hematopoietic cells (*Cxcr4*^{CreERT2}*;R26*^{Tomato}). **B**: Percentage of MDP-Mo in skull and femur bone marrow from 8-week old *Ms4a3*^{Cre}*;R26*^{Tomato} mice. n=5-6, from 3 experiments. Two-way ANOVA and Tukey's multiple comparisons test. **C**: Percentage of MDP-Mo from dura of *Ms4a3*$^{Cre/+}$*;R26*$^{Tomato/+}$ mice. Unpaired t-test, n=6-12, from 3 experiments. **D:** Representative flow cytometry plots showing histograms of MHC-II expression in MDP-Mo (blue) and GMP-Mo (orange). **E:** The difference in MHC-II

expression in MDP-Mo and GMP-Mo, measured as MFI from figure **D**. Paired t-test, n=6, from 2 experiments. **F:** UMAP representation based on scRNA-seq of sorted GMP-Mo and MDP-Mo from infected dura of *Ms4a3^{Cre};R26^{Tomato}* mice. n (mice)=4 from one experiment. The number of analyzed cells per condition is indicated. **G:** Normalized counts of *H2-Aa*, *Cd74* and *H2-Ab1* in MDP-Mo and GMP-Mo, from pseudo-bulk analysis. **H:** Volcano plot from pseudo-bulk analysis comparing DEG in MDP-Mo (right) and GMP-Mo (left)**,** padj<0.05 and $\log_2$(fold change)>0.5. The number of DEGs is indicated. **I:** Feature maps showing selected genes differentially upregulated in GMP-Mo (orange) or MDP-Mo (blue), while cells expressing both are marked in yellow. **J:** Heatmap comparing DEG from (*40*)(MDP-Mo and GMP-Mo from steady state bone marrow) with pseudo-bulk analysis from infected dura MDP-Mo and GMP-Mo. **K-L:** GO Terms for biological processes in GMP-Mo **(L)** or MDP-Mo **(M)**, with exclusions of the genes overlapping with GSE262369. Some GO Terms are represented, the complete list in Data file S1.

Fig. 5: Post-infection monocyte ontogeny diverges between dura and brain

A: Experimental setup for antibiotic treatment. Control mice were uninfected but received antibiotics. **B-D**: Monocyte (B), neutrophil (C) and dural macrophages (DM) (D) numbers in dura at 2, 7 and 30 dpi. One-way ANOVA with Tukey's test. n=5-14, from 4 experiments. **E-F:** Monocyte (E) and neutrophil (F) frequences in the brain and leptomeninges at 2, 7 and 30 dpi. Statistics by one-way ANOVA with Tukey's test. n=4-12, from 4 experiments. **G:** Flow cytometry showing MDP-Mo and GMP-Mo frequencies in dura over time (*Ms4a3^{Cre};R26^{Tomato}* mice, percentages in gates). **H-I**: Percentages of MDP-Mo among monocytes in dura. (**H**; n=5–12, 4 experiments) and in brain/leptomeninges (**I**; n=5–6, 3 experiments), analyzed by one-way ANOVA with Tukey's test. **J:** Representative flow cytometry plot showing MDP-Mo and GMP-Mo frequencies in brain and leptomeninges at 7 dpi, *Ms4a3^{Cre};R26^{Tomato}*mice. Percentages in gates. **K:** Sagittal brain section from *Ms4a3^{Cre};R26^{Tomato}*mice at 7 dpi. Anatomical location marked with red square on the overview image (right). Dasher rectangle represents the magnified picture. Arrows point to the parenchymal CD4 T cells. Scale bar (left)= 50 µm. Scale bar (right)= 10 µm. Scale bar (brain overview)= 1000 µm. **L:** Brain 7 dpi from *Ms4a3^{Cre};R26^{Tomato}* mouse. Letters on the overview image (left, scale bar= 1000 µm) represent anatomical location of magnified images on the right (scale bar=50 µm). **M:** Histogram and quantification of IFN-γ expression (left) or CD25 (right) of CD4 T cells cultured with either GMP-Mo or MDP-Mo. n=7, from 2 experiments. Paired t-test. **N:** Flow cytometry plots representing changes in Tomato^{+} and Tomato^{neg} dural macrophages over time, from *Ms4a3^{Cre};R26^{Tomato}* mice. **O:** Percentages of Tomato^{+} macrophages over time, *Ms4a3^{Cre};R26^{Tomato}* mice. One-way ANOVA with Tukey's test. n=5-12, from 4 experiments**. P:** Percentages of Tomato^{+} dural macrophages at 30 dpi, *Cxcr4^{CreERT2};R26^{Tomato}* mice. Unpaired t-test, n=3, from 2 experiments.

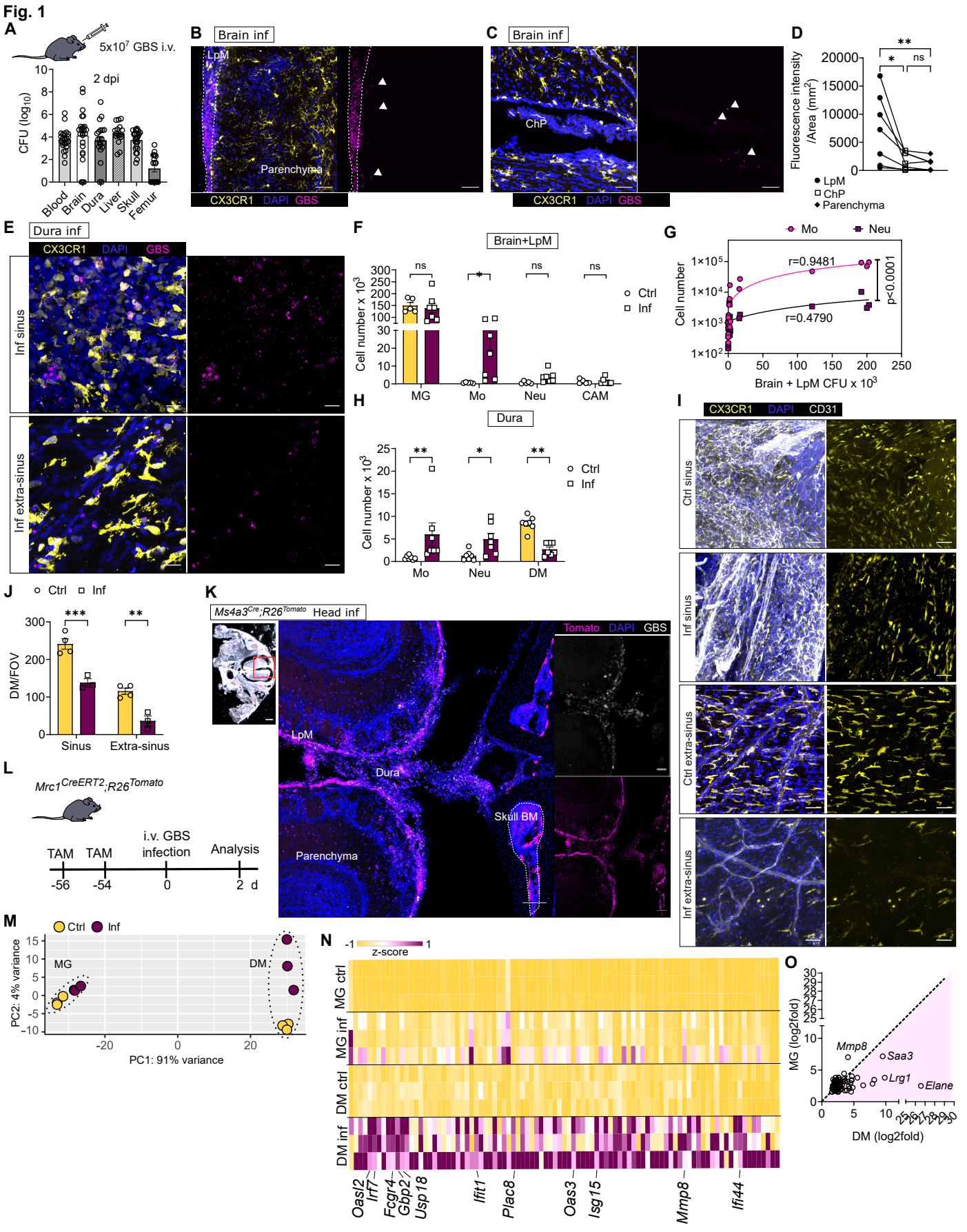
Fig. 1
A
5x10^7 GBS i.v.
2 dpi
CFU (log10)
Blood
Brain
Dura
Liver
Skull
Femur
B
Brain inf
LpM
Parenchyma
CX3CR1 DAPI GBS
C
Brain inf
ChP
CX3CR1 DAPI GBS
D
Fluorescence intensity /Area (mm2)
ns
LpM
ChP
Parenchyma
E
Dura inf
CX3CR1 DAPI GBS
Inf sinus
Inf extra-sinus
F
Brain+LpM
Cell number x 10^3
Ctrl
Inf
MG
Mo
Neu
CAM
G
Mo
Neu
r=0.9481
r=0.4790
p<0.0001
Cell number
Brain + LpM CFU x 10^3
H
Dura
Cell number x 10^3
Ctrl
Inf
Mo
Neu
DM
I
CX3CR1 DAPI CD31
Ctrl sinus
Inf sinus
Ctrl extra-sinus
Inf extra-sinus
J
Ctrl
Inf
DM/FOV
Sinus
Extra-sinus
K
Ms4a3Cre;R26Tomato Head inf
Tomato DAPI GBS
LpM
Dura
Skull BM
Parenchyma
L
Mrc1CreERT2;R26Tomato
TAM
TAM
i.v. GBS infection
Analysis
-56
-54
0
2 d
M
Ctrl
Inf
MG
DM
PC2: 4% variance
PC1: 91% variance
N
z-score
MG ctrl
MG inf
DM ctrl
DM inf
Oasl2
Irf7
Fcgr4
Gbp2
Usp18
Ifit1
Plac8
Oas3
Isg15
Mmp8
Ifi44
O
MG (log2fold)
DM (log2fold)
Mmp8
Saa3
Lrg1
Elane

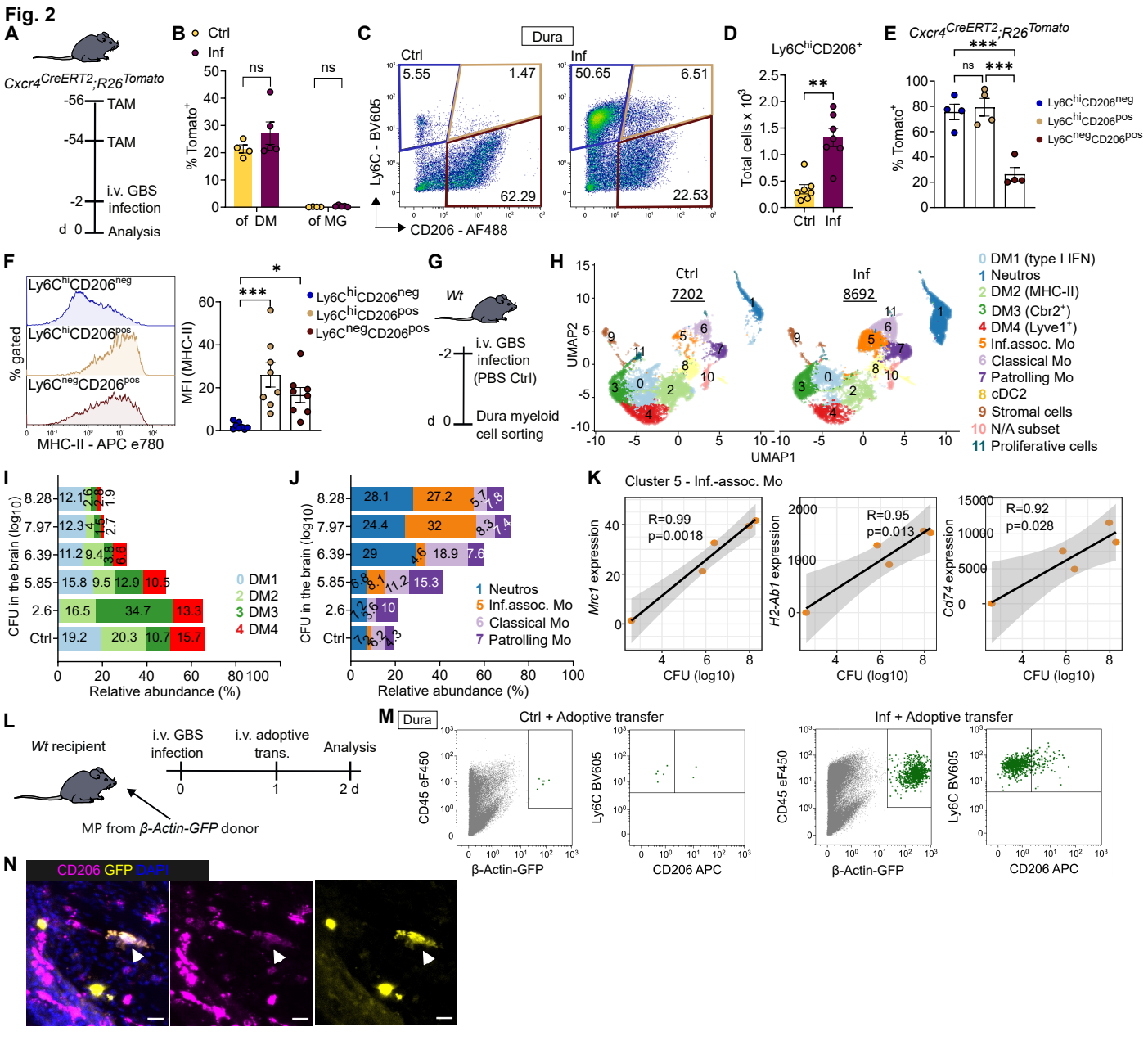
Fig. 2
A
Cxcr4CreERT2;R26Tomato
-56
TAM
-54
TAM
i.v. GBS infection
-2
d 0
Analysis
B
Ctrl
Inf
% Tomato+
ns
ns
of DM
of MG
C
Dura
Ctrl
Inf
5.55
1.47
62.29
50.65
6.51
22.53
Ly6C - BV605
CD206 - AF488
D
Ly6ChiCD206+
Total cells x 10^3
**
Ctrl
Inf
E
Cxcr4CreERT2;R26Tomato
***
ns
***
% Tomato+
Ly6ChiCD206neg
Ly6ChiCD206pos
Ly6cnegCD206pos
F
Ly6ChiCD206neg
Ly6ChiCD206pos
Ly6cnegCD206pos
% gated
MHC-II - APC e780
MFI (MHC-II)
***
*
G
Wt
-2
i.v. GBS infection (PBS Ctrl)
d 0
Dura myeloid cell sorting
H
Ctrl
7202
Inf
8692
UMAP2
UMAP1
0 DM1 (type I IFN)
1 Neutros
2 DM2 (MHC-II)
3 DM3 (Cbr2+)
4 DM4 (Lyve1+)
5 Inf.assoc. Mo
6 Classical Mo
7 Patrolling Mo
8 cDC2
9 Stromal cells
10 N/A subset
11 Proliferative cells
I
CFU in the brain (log10)
8.28
7.97
6.39
5.85
2.6
Ctrl
12.1
12.3
11.2
15.8
16.5
19.2
9.4
9.5
34.7
20.3
12.9
13.3
10.7
10.5
15.7
0 DM1
2 DM2
3 DM3
4 DM4
Relative abundance (%)
J
CFU in the brain (log10)
28.1
27.2
24.4
32
29
18.9
7.6
15.3
10
1 Neutros
5 Inf.assoc. Mo
6 Classical Mo
7 Patrolling Mo
Relative abundance (%)
K
Cluster 5 - Inf.-assoc. Mo
Mrc1 expression
R=0.99
p=0.0018
H2-Ab1 expression
R=0.95
p=0.013
Cd74 expression
R=0.92
p=0.028
CFU (log10)
L
Wt recipient
i.v. GBS infection
i.v. adoptive trans.
Analysis
0
1
2 d
MP from β-Actin-GFP donor
M
Dura
Ctrl + Adoptive transfer
Inf + Adoptive transfer
CD45 eF450
β-Actin-GFP
Ly6C BV605
CD206 APC
N
CD206 GFP DAPI

Fig. 3

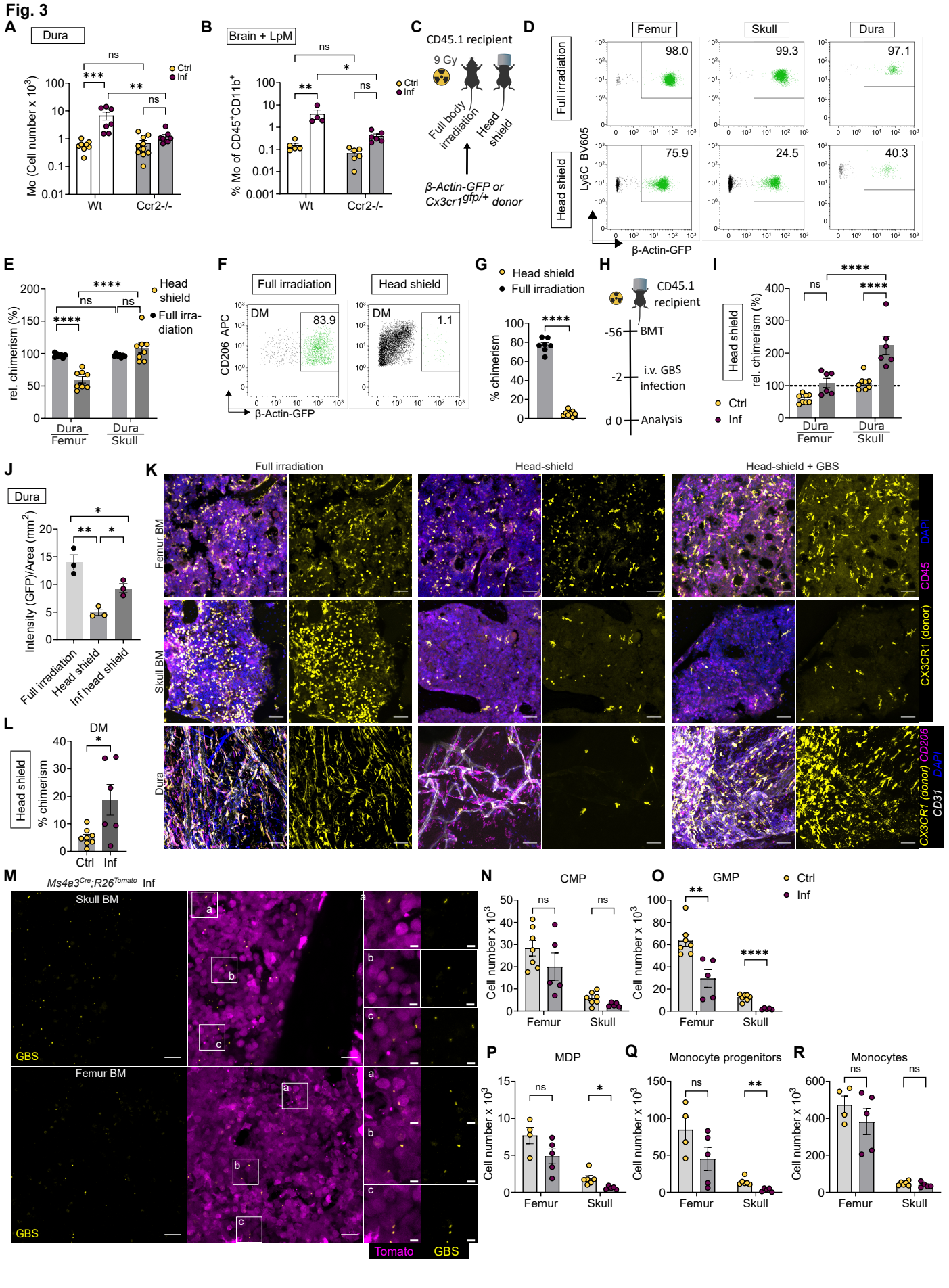
A
Dura
Mo (Cell number x 10^3)
Ctrl
Inf
ns
***
**
ns
Wt
Ccr2-/-
B
Brain + LpM
% Mo of CD45+CD11b+
ns
*
**
ns
Wt
Ccr2-/-
C
CD45.1 recipient
9 Gy
Full body irradiation
Head shield
β-Actin-GFP or Cx3cr1gfp/+ donor
D
Femur
Skull
Dura
Full irradiation
Head shield
98.0
99.3
97.1
75.9
24.5
40.3
Ly6C BV605
β-Actin-GFP
E
rel. chimerism (%)
Head shield
Full irradiation
****
ns
ns
****
Dura Femur
Dura Skull
F
Full irradiation
Head shield
DM
83.9
1.1
CD206 APC
β-Actin-GFP
G
Head shield
Full irradiation
% chimerism
****
H
CD45.1 recipient
-56
BMT
-2
i.v. GBS infection
d 0
Analysis
I
Head shield
rel. chimerism (%)
ns
****
****
Ctrl
Inf
Dura Femur
Dura Skull
J
Dura
Intensity (GFP)/Area (mm2)
*
**
*
Full irradiation
Head shield
Inf head shield
K
Full irradiation
Head-shield
Head-shield + GBS
Femur BM
Skull BM
Dura
DAPI
CD45
CX3CR1 (donor)
CX3CR1 (donor) CD206 DAPI CD31
L
Head shield
DM
% chimerism
*
Ctrl
Inf
M
Ms4a3Cre;R26Tomato Inf
Skull BM
Femur BM
GBS
Tomato
GBS
N
CMP
Cell number x 10^3
ns
ns
Femur
Skull
O
GMP
Ctrl
Inf
**
****
Femur
Skull
P
MDP
ns
*
Femur
Skull
Q
Monocyte progenitors
ns
**
Femur
Skull
R
Monocytes
ns
ns
Femur
Skull

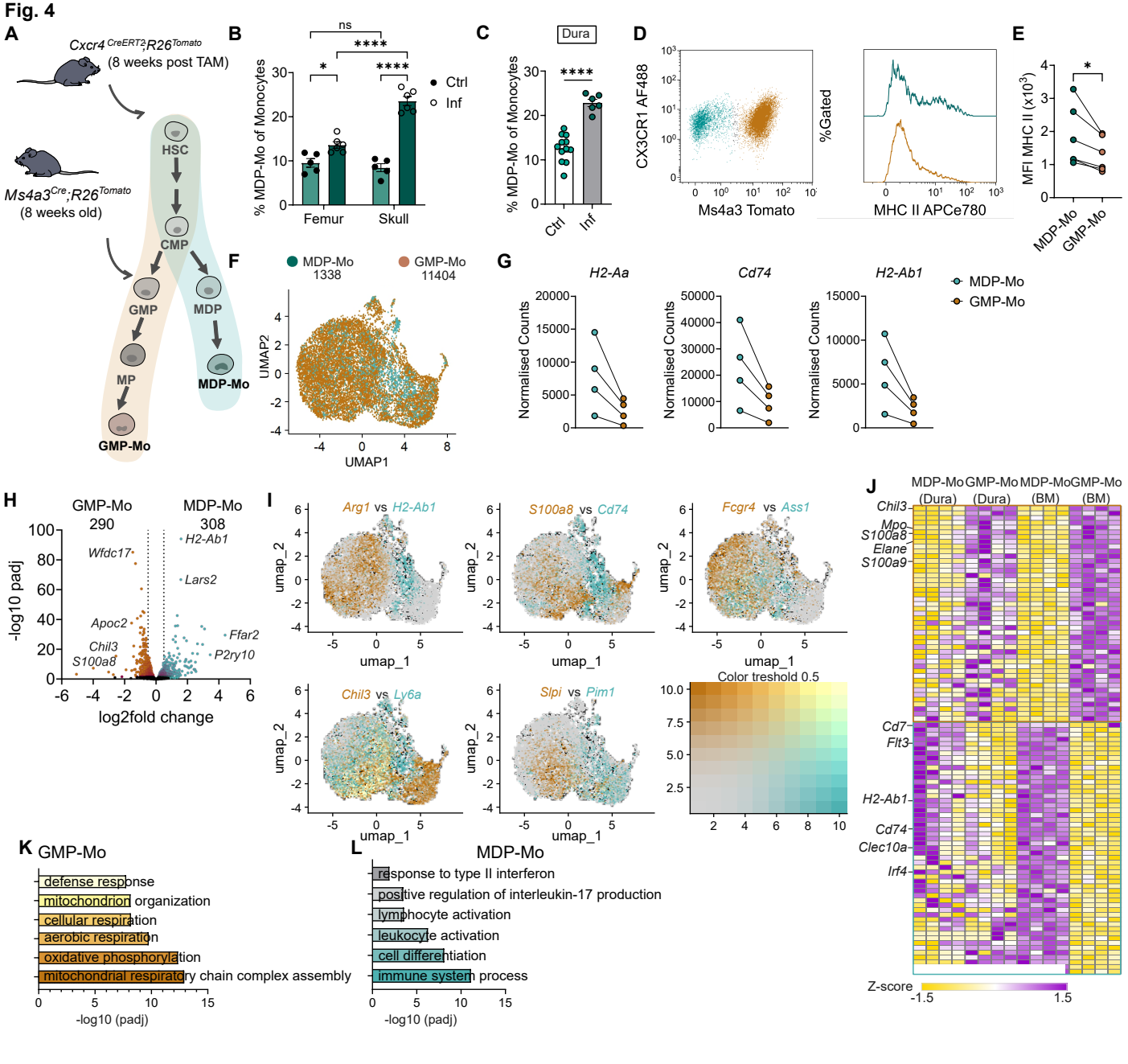
Fig. 4
A
Cxcr4 CreERT2;R26Tomato
(8 weeks post TAM)
Ms4a3Cre;R26Tomato
(8 weeks old)
HSC
CMP
GMP
MDP
MP
MDP-Mo
GMP-Mo
B
ns
****
*
****
% MDP-Mo of Monocytes
Ctrl
Inf
Femur
Skull
C
Dura
****
% MDP-Mo of Monocytes
Ctrl
Inf
D
CX3CR1 AF488
Ms4a3 Tomato
%Gated
MHC II APCe780
E
*
MFI MHC II (x10^3)
MDP-Mo
GMP-Mo
F
MDP-Mo
1338
GMP-Mo
11404
UMAP2
UMAP1
G
H2-Aa
Cd74
H2-Ab1
MDP-Mo
GMP-Mo
Normalised Counts
H
GMP-Mo
290
MDP-Mo
308
H2-Ab1
Wfdc17
Lars2
Apoc2
Ffar2
Chil3
P2ry10
S100a8
-log10 padj
log2fold change
I
Arg1 vs H2-Ab1
S100a8 vs Cd74
Fcgr4 vs Ass1
Chil3 vs Ly6a
Slpi vs Pim1
umap_1
umap_2
Color treshold 0.5
J
MDP-Mo (Dura)
GMP-Mo (Dura)
MDP-Mo (BM)
GMP-Mo (BM)
Chil3
Mpo
S100a8
Elane
S100a9
Cd7
Flt3
H2-Ab1
Cd74
Clec10a
Irf4
Z-score
-1.5
1.5
K
GMP-Mo
defense response
mitochondrion organization
cellular respiration
aerobic respiration
oxidative phosphorylation
mitochondrial respiratory chain complex assembly
-log10 (padj)
L
MDP-Mo
response to type II interferon
positive regulation of interleukin-17 production
lymphocyte activation
leukocyte activation
cell differentiation
immune system process
-log10 (padj)

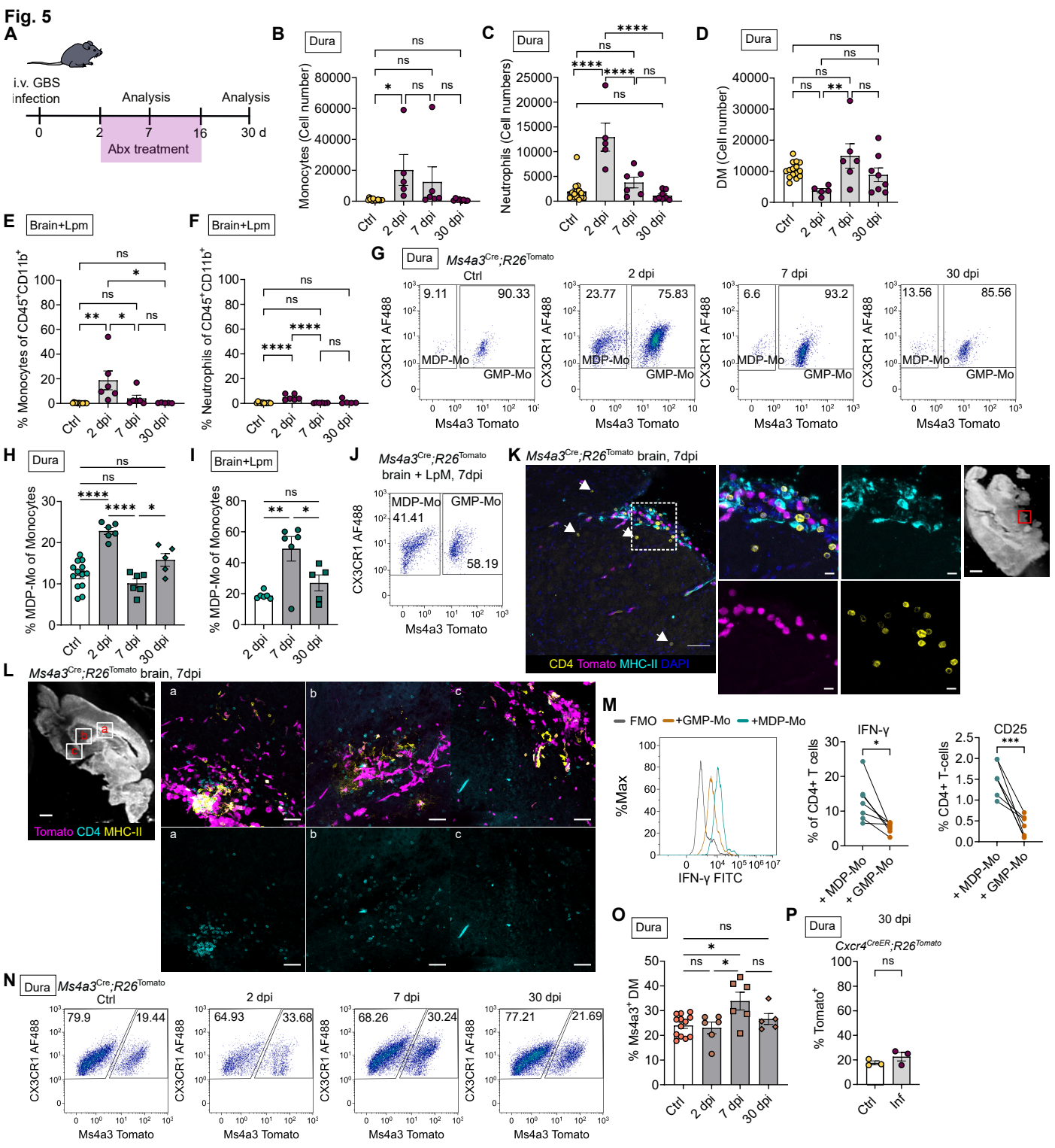
Fig. 5
A
i.v. GBS infection
Analysis
Analysis
0
2
7
16
30 d
Abx treatment
B
Dura
Monocytes (Cell number)
Ctrl
2 dpi
7 dpi
30 dpi
C
Dura
Neutrophils (Cell numbers)
D
Dura
DM (Cell number)
E
Brain+Lpm
% Monocytes of CD45+CD11b+
F
Brain+Lpm
% Neutrophils of CD45+CD11b+
G
Dura
Ms4a3Cre;R26Tomato
Ctrl
2 dpi
7 dpi
30 dpi
9.11
90.33
23.77
75.83
6.6
93.2
13.56
85.56
MDP-Mo
GMP-Mo
CX3CR1 AF488
Ms4a3 Tomato
H
Dura
% MDP-Mo of Monocytes
I
Brain+Lpm
% MDP-Mo of Monocytes
J
Ms4a3Cre;R26Tomato
brain + LpM, 7dpi
MDP-Mo
41.41
GMP-Mo
58.19
CX3CR1 AF488
Ms4a3 Tomato
K
Ms4a3Cre;R26Tomato brain, 7dpi
CD4 Tomato MHC-II DAPI
L
Ms4a3Cre;R26Tomato brain, 7dpi
a
b
c
Tomato CD4 MHC-II
M
FMO
+GMP-Mo
+MDP-Mo
%Max
IFN-γ FITC
IFN-γ
% of CD4+ T cells
+ MDP-Mo
+ GMP-Mo
CD25
% CD4+ T-cells
N
Dura
Ms4a3Cre;R26Tomato
Ctrl
2 dpi
7 dpi
30 dpi
79.9
19.44
64.93
33.68
68.26
30.24
77.21
21.69
CX3CR1 AF488
Ms4a3 Tomato
O
Dura
% Ms4a3+ DM
Ctrl
2 dpi
7 dpi
30 dpi
P
Dura
30 dpi
Cxcr4CreER;R26Tomato
% Tomato+
Ctrl
Inf

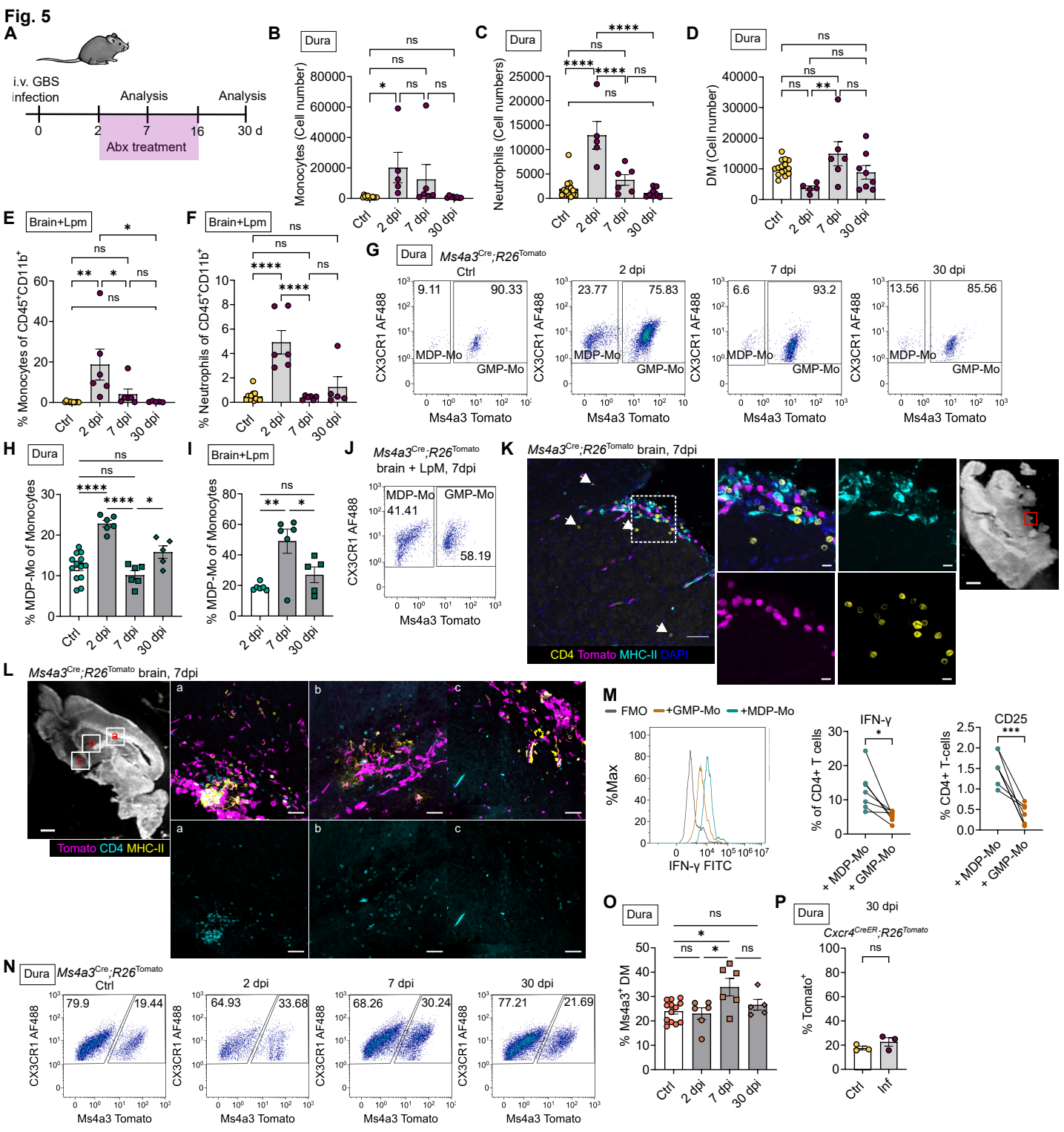
Fig. 5
A
i.v. GBS infection
Analysis
Analysis
0
2
7
16
30 d
Abx treatment
B
Dura
Monocytes (Cell number)
Ctrl
2 dpi
7 dpi
30 dpi
C
Dura
Neutrophils (Cell numbers)
D
Dura
DM (Cell number)
E
Brain+Lpm
% Monocytes of CD45+CD11b+
F
Brain+Lpm
% Neutrophils of CD45+CD11b+
G
Dura
Ms4a3Cre;R26Tomato
Ctrl
2 dpi
7 dpi
30 dpi
CX3CR1 AF488
Ms4a3 Tomato
MDP-Mo
GMP-Mo
9.11
90.33
23.77
75.83
6.6
93.2
13.56
85.56
H
Dura
% MDP-Mo of Monocytes
I
Brain+Lpm
% MDP-Mo of Monocytes
J
Ms4a3Cre;R26Tomato
brain + LpM, 7dpi
MDP-Mo
41.41
GMP-Mo
58.19
K
Ms4a3Cre;R26Tomato brain, 7dpi
CD4 Tomato MHC-II DAPI
L
Ms4a3Cre;R26Tomato brain, 7dpi
Tomato CD4 MHC-II
M
FMO
+GMP-Mo
+MDP-Mo
%Max
IFN-γ FITC
IFN-γ
% of CD4+ T cells
+ MDP-Mo
+ GMP-Mo
CD25
% CD4+ T-cells
N
Dura
Ms4a3Cre;R26Tomato
Ctrl
2 dpi
7 dpi
30 dpi
79.9
19.44
64.93
33.68
68.26
30.24
77.21
21.69
O
Dura
% Ms4a3+ DM
P
Dura
30 dpi
Cxcr4CreER;R26Tomato
% Tomato+
Ctrl
Inf

Supplementary Methods

Mice

Mice were bred in animal facilities of the University of Freiburg under specific pathogen-free conditions and were kept in groups of a maximum five animals per cage at defined environmental conditions. Food and water were available *ad libitum*, and day/night cycles were set to 12 h. All animal experiments were approved by the Federal Ministry for Nature, Environment and Consumer's protection of the state of Baden-Wuerttemberg (proposal numbers G-19/031 and G23/008).

GBS culturing

GBS strain BM110 was streaked on blood agar plates (Columbia agar + 5% sheep blood; BioMérieux) and incubated overnight at 37°C. A single colony was inoculated into 5 ml Todd–Hewitt broth and cultured overnight at 37°C, then diluted into 200 ml warm Todd–Hewitt broth and grown to mid-log phase. Bacterial concentration was determined by optical density (OD600 = 0.4) and confirmed by serial dilution plating on blood agar plates. Bacteria were washed twice with PBS and resuspended to 10^9 CFU/ml.

CFU assay

Mice were euthanized by CO_2 inhalation and blood was collected by cardiac puncture. Mice were transcardially perfused with ice-cold sterile PBS. Liver, spleen, and brain were collected in sterile bags and mechanically dissociated. Femoral bone marrow was flushed through a 70 µm cell strainer with 2.5–3 ml sterile PBS, and 20 µl of suspension was plated on Granada agar (BD). Skull marrow was extracted as previously described (*12*), with minor modifications. After dura removal, the calvarium was cut into small pieces in 1 ml sterile PBS and plated on Granada agar. Dura was digested for 20 min at 37°C with shaking in 1 ml RPMI containing 2.5 mg collagenase IV, and 20 µl of suspension or serial dilutions were plated on Granada agar. Tissues from control animals were plated in parallel to confirm sterility, with no bacterial growth detected.

Flow cytometry:

For calculating absolute numbers of cells in dura, the whole dura was acquired. For calculating absolute numbers of populations in brain, skull or femur, a defined volume of the processed tissue was acquired for a pre-defined time (30-60s) at a flow of 10 µL/min or 30 µL/min. Antibodies used for stainings are as follows:

anti-mouse CD3e APC Clone 145-2C11 (BioLegend) 1:500
anti-mouse CD4 PerCP-Cy5.5 Clone RM4-5 (eBioscience) 1:800
anti-mouse CD16/32 PE Cy7 Clone 93 (eBioscience) 1:100
anti-mouse CD19 APC Clone 1D3/CD19 (BioLegend) 1:200
anti-mouse CD25 APC Clone PC61 (BioLegend) 1:100
anti-mouse CD34 PE Clone HM34 (BioLegend) 1:100
anti-mouse CD45 APC Clone 30-F11 (BioLegend) 1:300
anti-mouse CD45 eFluor450 Clone 30-F11 (eBioscience) 1:300
anti-mouse CD45 FITC Clone 30-F11 (eBioscience) 1:100
anti-mouse CD45 PerCP Cy5.5 Clone 30-F11 (eBioscience) 1:500
anti-mouse CD45.1 FITC Clone A20 (eBioscience) 1:200
anti mouse CD45.2 PerCP Cy5.5 Clone 104 (eBioscience) 1:400
anti mouse CD11b FITC Clone REA592 (Miltenyi) 1:100
anti-mouse CD11b PE-Cy7 Clone M1/70 (eBioscience) 1:3000
anti-mouse CD11b APC-eFlour780 Clone M1/70 (eBioscience) 1:3000
anti-mouse CD117 BV421 Clone 2B8 (BioLegend) 1:100
anti-mouse CD117 PE Cy7 Clone 2B8 (eBioscience) 1:500
anti-mouse CD115 PE Clone AFS98 (BioLegend) 1:50
anti-mouse CD115 APC Clone AFS98 (Miltenyi) 1:100
anti-mouse CD115 BV421 Clone AFS98 (BioLegend) 1:100
anti-mouse CD127 APC Clone A7R34 (BioLegend) 1:100
anti-mouse CD206 APC Clone C068C2 (BioLegend) 1:200
anti-mouse CD206 PE Clone C068C2 (BioLegend) 1:200
anti-mouse CD206 AF488 Clone C068C2 (BioLegend) 1:200

anti-mouse CD206 PE Clone C068C2 (BioLegend) 1:200
anti-mouse CX3CR1 AF488 Clone SA011F11 (BioLegend) 1:100
anti-mouse Ly6G FITC Clone 1A8 (BD Pharmingen) 1:200
anti-mouse Ly6G AF488 Clone 1A8 (BioLegend) 1:200
anti-mouse Ly6G PE Clone 1A8 (BD) 1:500
anti-mouse Ly6G APC Clone 1A8 (BD Pharmingen) 1:200
anti-mouse Ly6c PerCp-Cy5.5 Clone HK1.4 (Invitrogen) 1:500
anti-mouse Ly6C BV605 Clone HK1.4 (BioLegend) 1:200
anti-mouse MHC II APC eFlour780 Clone M5/114.15.2 (eBioscience) 1:200
anti-mouse Ter119 APC Clone TER-119 (BioLegend) 1:200
anti-mouse Sca-1 AF488 Clone D7 (BioLegend) 1:100
anti-mouse IFN-γ FITC Clone XMG1.2 (BioLegend) 1:100
anti-mouse B220 PE Clone RA3-6B2 (eBioscience) 1:100
anti-mouse CD8a PE Clone 53-6.7 (eBioscience) 1:100

Adoptive transfer

Bone marrow was isolated from tibiae and femora of *β-Actin-gfp*$^{+/-}$ mice, flushed with sterile ice-cold PBS and centrifuged for 6 min at 1500 rpm. Cells were resuspended in 1% BSA in PBS, stained and sorted as described above. Sorted monocyte progenitors were resuspended in PBS + 2% murine serum obtained from the donor mice. Monocyte progenitors were injected intravenously at 1 dpi (~2–4 × 10^5/animal). Recipients were analyzed 1 day post transfer (2 days post infection). Blood, brain, dura and bone marrow (from femur and skull) were analyzed on a flow cytometer (Gallios™, Beckman Coulter) and processed with the Kaluza software (v2.1, Beckman Coulter) and/or microscopy.

ELISA

One brain hemisphere was weighed and stored in 1 ml of homogenization buffer (50 mM Tris pH 8, 150 mM NaCl, 5 mM EDTA) containing 10 µl phosphatase and protease inhibitors (Pierce). Brain was homogenized using tissue lyser (Quiagen^{TM} TissueLyser) with 50/s oscillations for 5 min with 3 mm tungsten carbide beads. Tissue debris was removed by centrifugation at 20 000 g for 10 min at 4°C. Supernatants were kept at -80°C until the analysis. For plasma ELISA, blood was collected into Microvette® tube (Sarstedt) and centrifuged at 10 000 g for 10 min. Plasma was collected and kept at -80°C until the analysis. Concentrations of IL-6, TNF, IL-1β and IFN-β were measured using mouse R&D Duo set ELISA kits according to the manufacturer's instructions (R&D Systems).

Bulk RNA sequencing

Sequencing was performed with 2 x 100 bp read length and 50 million clusters/probe on NovaSeq 6000 (Illumina). Raw data was provided by CeGat. Group comparison was done using DESeq2 in R. PCA plots were done using DESeq2 in R 4.3.3 and RStudio version 2023.12.1. GO terms were analyzed with the online tool "g:Profiler"(*60*). Heat maps were made using Morpheus (*61*).

Single-cell RNA sequencing downstream analysis

For myeloid population scSeq from control and infected dura, downstream analyses were conducted in the R version 4.2.0 programming environment using the Seurat package version 4. Cells were retained if the mitochondrial gene content was below 5%. To exclude empty droplets or doublets we limited the number of detected genes per cell between 200 and 5,000. Total counts per cell had to exceed 500 to ensure a minimum level of transcriptional activity indicative of viable cells.

In addition, we filtered out specific classes of genes that can introduce potential biases by overrepresentation of ribosomal or pseudogenes in the scRNAseq data. Genes belonging to the murine-specific ribosomal protein large (Gm) family, and ribosomal proteins (Rpl and Rps), were excluded. These genes were identified using regular expressions to match gene names starting with "Gm", "Rpl", or "Rps" and were removed from the analysis.

Data was integrated from two separate experiments using the SCtransform algorithm within Seurat. 2000 features were identified using SelectIntegrationFeatures() and used in PrepSCTIntegration() and FindIntegrationAnchors(). These anchors were used on IntegrateData(). The top 30 PCAs were used for Umap calculation. FindNeighbors() and FindClusters() were calculated with the top 30 dimensions each. For the

latter, a resolution of 0.299 was chosen as the highest resolution where every cluster was distinguishable by specific biological functions. Core markers were identified using the FindAllMarkers functions using a threshold of at least 25% of cells expressing the gene and only returning positive values. All clusters are displayed in the respective Violin plots generated by VlnPlot() and sorted according to the respective median. For monocyte scSeq (GMP-Mo and MDP-Mo), downstream analyses were conducted in R version 4.5.1 programming environment using the Seurat package version 5.3.1. Cells were retained only if the mitochondrial gene content was below 20% and we restricted the number of detected genes per cell to be between 300 and 6,000. Furthermore, total UMI counts per cell were required to exceed 500.
In addition to cell-level filtering, we removed specific classes of genes that could introduce bias due to overrepresentation in scRNA-seq datasets. Genes corresponding to mitochondrial transcripts were identified using the regular expression pattern "(?i)^mt-", and ribosomal protein genes were detected using the pattern "(?i)^(rpl|rps)". To compare transcriptional profiles between MDP-Mo and GMP-Mo populations, pseudobulk function was used, in which counts from individual cells belonging to the same sample and lineage were aggregated to generate sample-level expression profiles. Pseudobulk count matrices were generated for each sample × lineage combination, normalized, and analyzed using DESeq2. DEG were defined as $p<0.05$, logFold2(Change)>0.5. For comparison with bulk RNA seq data from GSE262369, published data was analysed using DESeq2, in which DEG were defined as $p<0.05$, logFold2(Change)>0.5. Heat maps were made using Morpheus (*61*).

Immunofluorescence labelling

Dilutions of antibodies were 1:500 for Iba-1 (WACO, Japan), 1:200 for anti-GBS (Invitrogen), 1:100 for CD4 – AF488 (BioLegend), 1:100 for CD4 – Pacific Blue (BioLegend), 1:100 for CD74 – AF647 (BioLegend), 1:200 for CD206 – PE (BioLegend), 1:100 for CD206- APC (Biolegend), 1:100 for CD45-PE (Invitrogen), 1:100 for CD31-PE (BD Pharmigen) and 1:50 for MHC-II APC (Miltenyi). After washing 5x with PBS, samples are incubated for 2h at RT with secondary antibody (goat anti-rabbit Alexa Fluor633 1:500, anti-GFP DyLight488 1:1000 for enhancing endogenous signal in Cx3Cr1/gfp mice) and DAPI (1:1000).

Sorting of T cells

Deep cervical lymph nodes were collected from infected mice at 7 dpi. They were mechanically pushed through 70 µm cell strainer into a canonical tube using sterile FACS buffer. Cells were washed and stained as described in Methods, after which they were FACS sorted into co-culture medium (RPMI, 25 µM 2-mercaptoethanol, 10% FBS and 0.5% Ciprofloxacin).

T cell co-culture and stimulation

MDP-Mo and GMP-Mo were isolated from femur and tibia of *Ms4a3^{Cre};R26^{Tomato}* mice, stained and FACS-sorted as described above. 20 000 cells per well were put in culture medium (RPMI, 10% FBS, 0.5% Ciprofloxacin, 10 mg/mL M-CSF) into 96-flat bottom plate. 16h later cells were stimulated with $5x10^7$ heat-fixed GBS/ml for 2h. Cells were thoroughly washed and 100 000 CD4 T cells were added. Medium used for co-culture had RPMI, 25 µM 2-mercaptoethanol, 10% FBS and 0.5% Ciprofloxacin.
After 24 h, T cells were analyzed by flow cytometry. For IFN-γ intracellular staining, cells were treated with protein transport inhibitor (BD GolgiStop™) at 0.67 µl/mL for 2 h before the fixation and permeabilization. Intracellular staining was done using Intracellular Fixation & Permeabilization Buffer Set (eBioscience) according to manufacturer's instructions.

Fig. S1

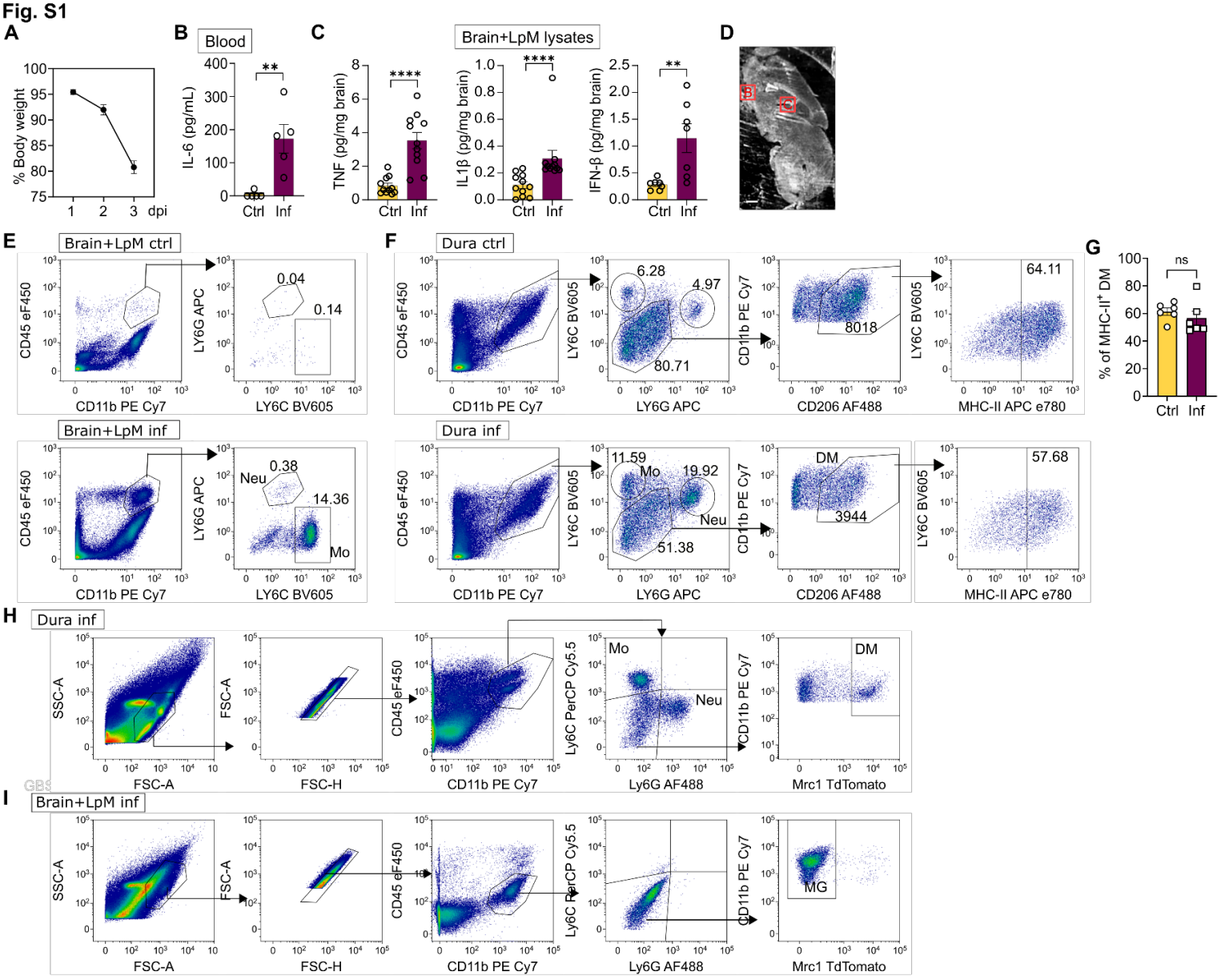

Fig. S1: A: Weight loss curve in the first three days of the infection, for 1 dpi n=20, for 2 dpi n=23 and for 3 dpi n=8, from 3 experiments. **B**: IL-6 in plasma 2 dpi, n=5. Statistics by Mann-Whitney U-test, from 2 independent experiments. **C:** TNF, IL-1β and IFN-β ELISA from homogenized brains. Measured values are normalized with the brain mass in mg. For IFN-β n=7, TNF and IL-1β n=11. Statistics by Mann-Whitney U-test from 3-4 experiments. **D:** Overview image of the brain positions corresponding to Fig. 1 B, C. Scale bar=1000 µm. **E-F**: Representative flow cytometry plots of percentage of monocytes and neutrophils in control and infected (**E**) brain and leptomeninx (LpM) or (**F**) dura. In **E**, numbers indicate percentages of the population, out of all myeloid cells. In **F**, numbers represent percentages of monocytes (Mo) and neutrophils (Neu), numbers of dural macrophages (DM), and percentages of MHC-II positive dural macrophages. **G:** Comparison of % of MHC-II positive dural macrophages in control and infected mice, n= 6, from 3 independent experiments, unpaired t-test. **H-I:** Representative flow cytometry gating used for sorting dural macrophages (**H**) and microglia (MG) (**I**) from dura and brain of *Mrc1*^{CreERT2}*;R26*^{Tom} mice for bulk RNA sequencing.

Fig. S2

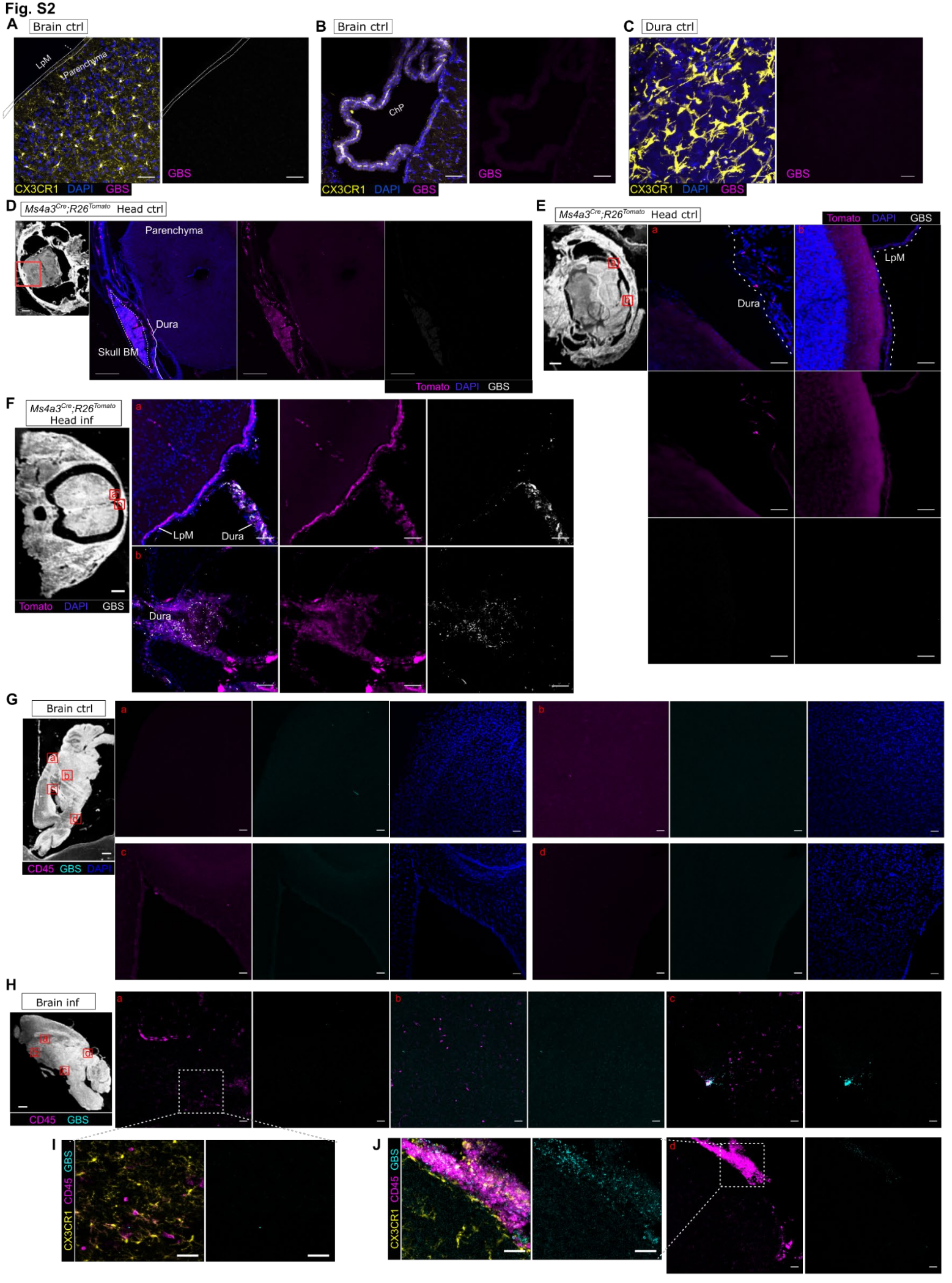
A
Brain ctrl
LpM
Parenchyma
CX3CR1 DAPI GBS
GBS
B
Brain ctrl
ChP
CX3CR1 DAPI GBS
GBS
C
Dura ctrl
CX3CR1 DAPI GBS
GBS
D
Ms4a3Cre;R26Tomato Head ctrl
Parenchyma
Dura
Skull BM
Tomato DAPI GBS
E
Ms4a3Cre;R26Tomato Head ctrl
Tomato DAPI GBS
a
b
Dura
LpM
F
Ms4a3Cre;R26Tomato
Head inf
Tomato DAPI GBS
a
b
LpM
Dura
Dura
G
Brain ctrl
CD45 GBS DAPI
a
b
c
d
H
Brain inf
CD45 GBS
a
b
c
I
CX3CR1 CD45 GBS
J
CX3CR1 CD45 GBS
d

Fig. S2: A-B: Representative maximal intensity projection of sagittal brain slices of control *Cx3cr1*$^{gfp/+}$ mice including leptomeningeal area (LpM) and parenchyma (**D**) or choroid plexus (ChP) (**E**) stained with GBS-AF633 (magenta) and DAPI (blue). Scale bar=50 µm. **C:** Representative maximal intensity projection of extra-sinusoidal region of whole mount control dura from *Cx3cr1*$^{gfp/+}$ mouse, stained with GBS-AF633 (magenta) and DAPI (blue). Scale bar = 20 µm. **D:** Representative image of a coronal slice of control *Ms4a3*^{Cre}*;R26*^{Tomato} mouse, stained with DAPI (blue), and GBS-AF633 (white). Scale bar (left)=1000 µm. Scale bar (right)=500 µm. **E-F:** Coronal slice of control (**E**) or infected (**F**) *Ms4a3*^{Cre}*;R26*^{Tomato} mouse, stained with DAPI (blue), and GBS-AF633 (white). Anatomical location is indicated (letters) on head's overview image (left). Dura and LpM indicated. Scale bar (left)=1000 µm. Scale bar (right)=50 µm. **G-H**: CD45^{+} immune cell and GBS distribution in control (**G**) and infected (**H**) brains. The overview image (left) indicates the anatomical locations (letters) from which higher-magnification images (right) were acquired. Scale bar (left) =1000 µm, scale bar (right) =50 µm. **I-J:** Higher magnification images from **H**, showing immune cell influx into parenchyma (**I**) and accumulation in the leptomeninges (**J**). Scale bar=50 µm.

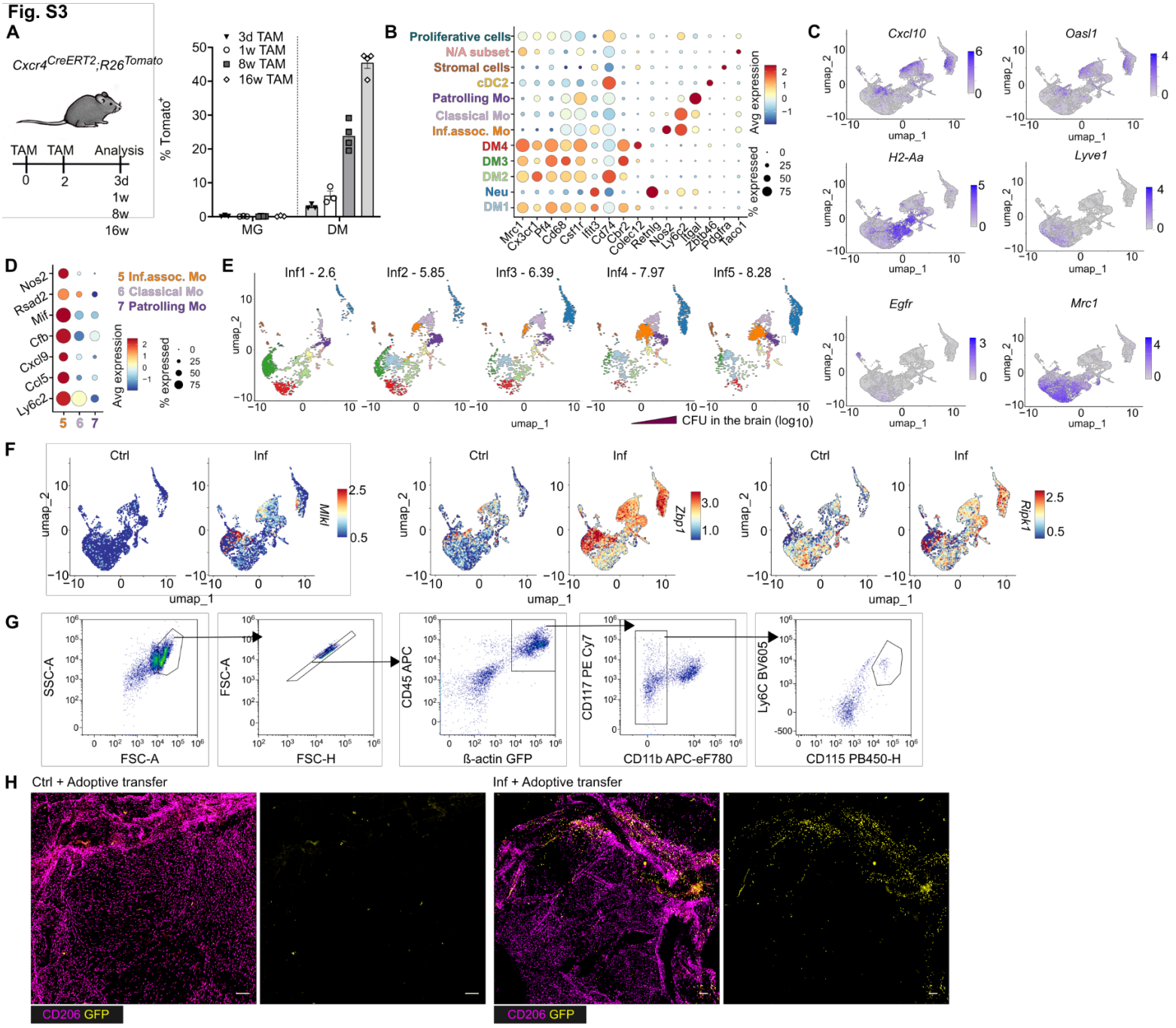

Fig. S3: A: *Cxcr4*^{CreERT2}*;R26*^{Tomato} mice were induced for 3 days, 1, 8 or 16 weeks, recombination in dural macrophages (DM) and microglia (MG) was measured as a percentage of Tomato positive CD45^{hi}CD11b^{+}Ly6G^{neg}CD206^{+} macrophages in dura or CD45^{lo}CD11b^{+}Ly6C^{neg}Ly6G^{neg}CD206^{neg} microglia in brain. n=3-4, from 3 experiments. **B:** Dotplot representing selected discriminatory genes between different clusters. Color represents the mean expression of the gene and the dot size represents the percentage of the cells expressing the gene in each cluster. **C:** Featureplot representing selected genes upregulated in each of the dural macrophage clusters. **D:** Dotplot representing some inflammation-associated genes expressed in infection-associated monocytes, in comparison to classical and patrolling monocytes. Color represents the mean expression of the gene and the dot size represents the percentage of the cells expressing the gene in each cluster. **E:** UMAP clustering of individual infected mice from least bacterial burden in the brain (inf1) to most (inf5) show burden-related inf-assoc. monocyte (cluster 5) and neutrophil (cluster 1) influx, in parallel with dural macrophage disappearance (clusters 0, 2, 3, 4). **F:** Feature plots of canonical necroptosis genes expressed in control and infected condition. **G:** Gating strategy for sorting monocyte progenitors from bone marrow of *ß-actin-GFP* mice for adoptive transfer. **H:** Representative image of whole mount dura, either control and infected, with donor-derived cells marked in yellow. Scale bar=200 µm.

Fig. S4

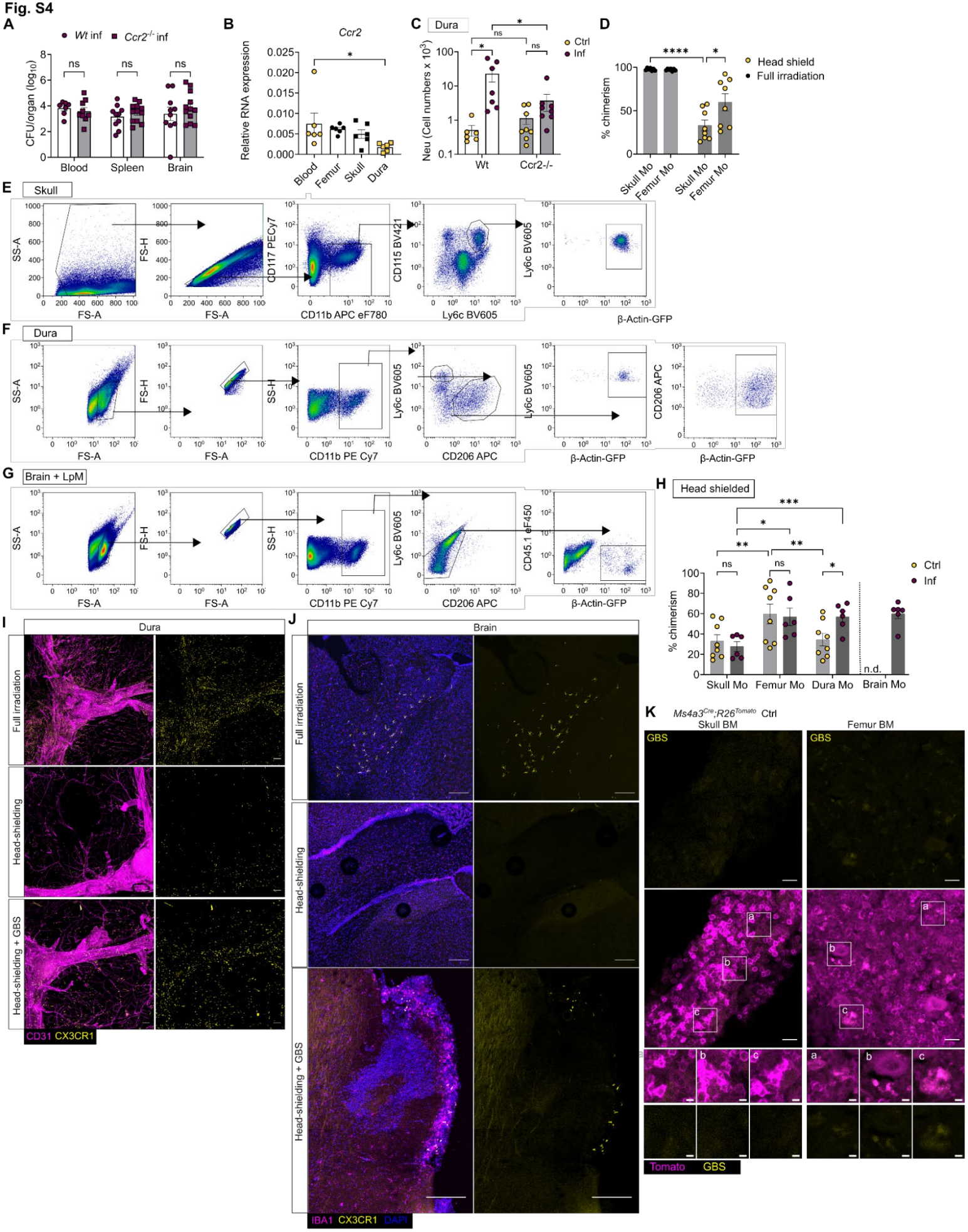
A
Wt inf
Ccr2-/- inf
CFU/organ (log10)
ns
Blood
Spleen
Brain
B
Ccr2
Relative RNA expression
Blood
Femur
Skull
Dura
C
Dura
Neu (Cell numbers x 10^3)
Ctrl
Inf
Wt
Ccr2-/-
D
% chimerism
Head shield
Full irradiation
Skull Mo
Femur Mo
E
Skull
SS-A
FS-A
FS-H
CD117 PECy7
CD11b APC eF780
CD115 BV421
Ly6c BV605
β-Actin-GFP
F
Dura
SS-H
CD11b PE Cy7
CD206 APC
G
Brain + LpM
CD45.1 eF450
H
Head shielded
Dura Mo
Brain Mo
n.d.
I
Dura
Full irradiation
Head-shielding
Head-shielding + GBS
CD31 CX3CR1
J
Brain
IBA1 CX3CR1 DAPI
K
Ms4a3Cre;R26Tomato Ctrl
Skull BM
Femur BM
GBS
Tomato

Fig. S4: A: CFU from blood, spleen and brain of infected *Wt* or *Ccr2*$^{-/-}$ *mice*, n=7-12 from 4 experiments. Multiple U-tests followed by Holm-Šídák. **B:** *Ccr2* expression measured by qPCR from monocytes sorted from steady-state blood, femur, skull and dura (n=6) of *Wt* mice from 2 experiments. One-way ANOVA and Tukey's test. **C:** Flow cytometry analysis of neutrophils in dura of control and infected *Wt* or *Ccr2*$^{-/-}$ mice. Two-way ANOVA and Tukey's test (n=8-9, from 4 experiments). **D:** Percentage chimerism in head shielded or fully irradiated monocytes from skull or femur, measured by flow cytometry. Two-way ANOVA and Tukey's test. n=7-8 from 4 experiments. **E-G**: Representative flow cytometry gating of donor-derived monocytes in skull (**E**), donor-derived monocytes and macrophages in dura (**F**) and donor-derived microglia in brain and leptomeninx (LpM) (**G**) of fully irradiated mice. **H:** Chimerism of monocytes in skull, femur, dura and brain of control and infected head-shielded chimeras. Two-way ANOVA followed by Tukey's test, n=6-8, from 4 experiments. Brain monocytes were excluded from statistical analysis, due to low numbers of monocytes in steady state brains. n.d. = not determined. **I:** Representative images of whole-mounted dura from either fully irradiated and head shielded controls, or head shielded infected mice. Donors were *Cx3cr1*$^{+/gfp}$ mice. Donor derived cells are in yellow. Scale bar = 200 µm. **J:** Representative images of brain sagittal sections from either fully irradiated and head shielded controls, or head shielded infected mice. Donors were *Cx3cr1*$^{+/gfp}$ mice. Donor derived cells are in yellow. Scale bar = 200 µm. **K:** Femur and skull bone marrow from control *Ms4a3*^{Cre}*;R26*^{Tomato} mice stained with GBS-AF633. Scale bar(upper image)=20 µm, (lower image)=5 µm.

Fig. S5

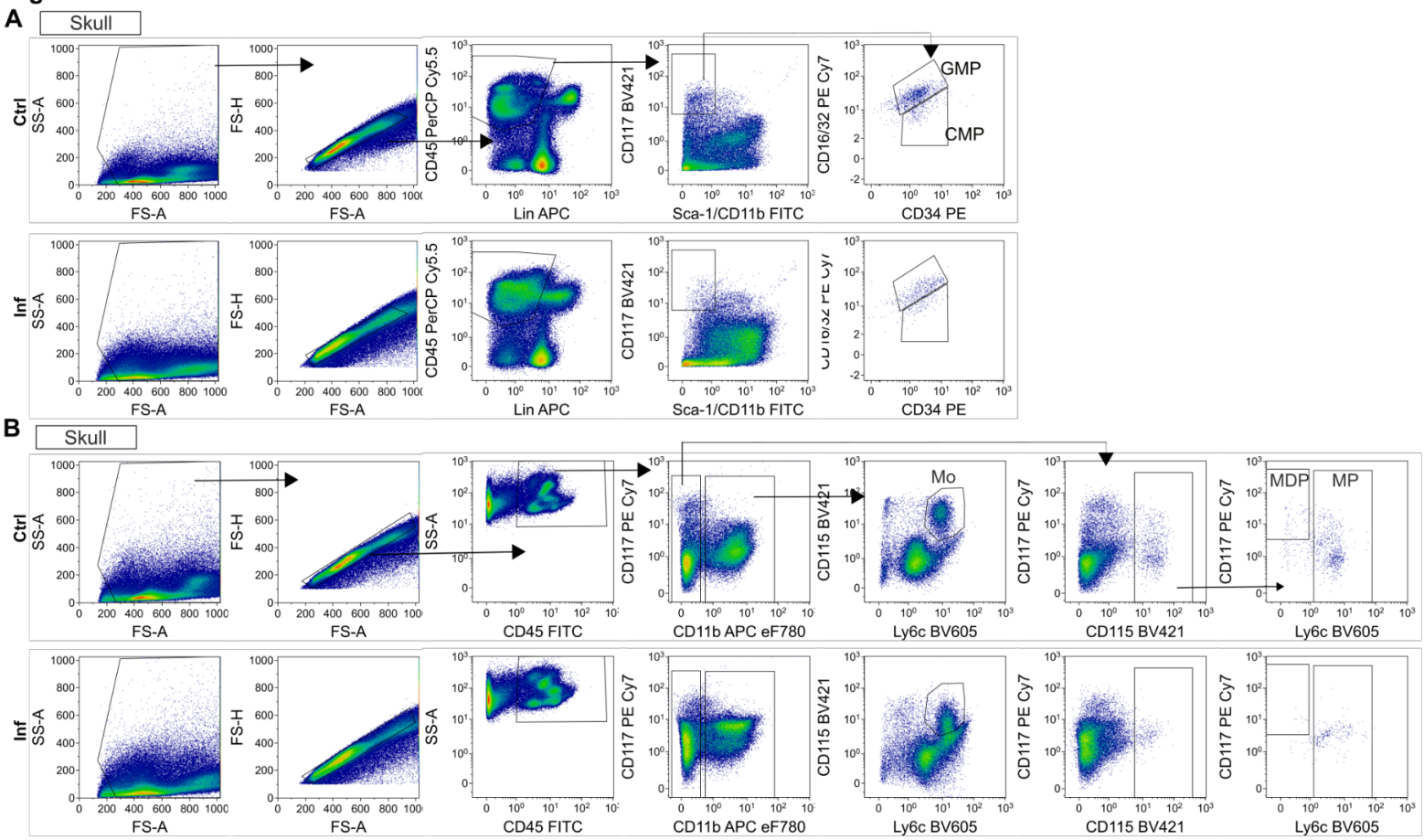

Fig. S5: Gating strategy

A: Representative flow cytometry plots showing the gating strategy for CMP and GMP in control and infected skull bone marrow. **B:** Representative flow cytometry plots showing the gating strategy for monocytes (Mo), MDP and monocyte progenitors (MP) in control and infected skull bone marrow.

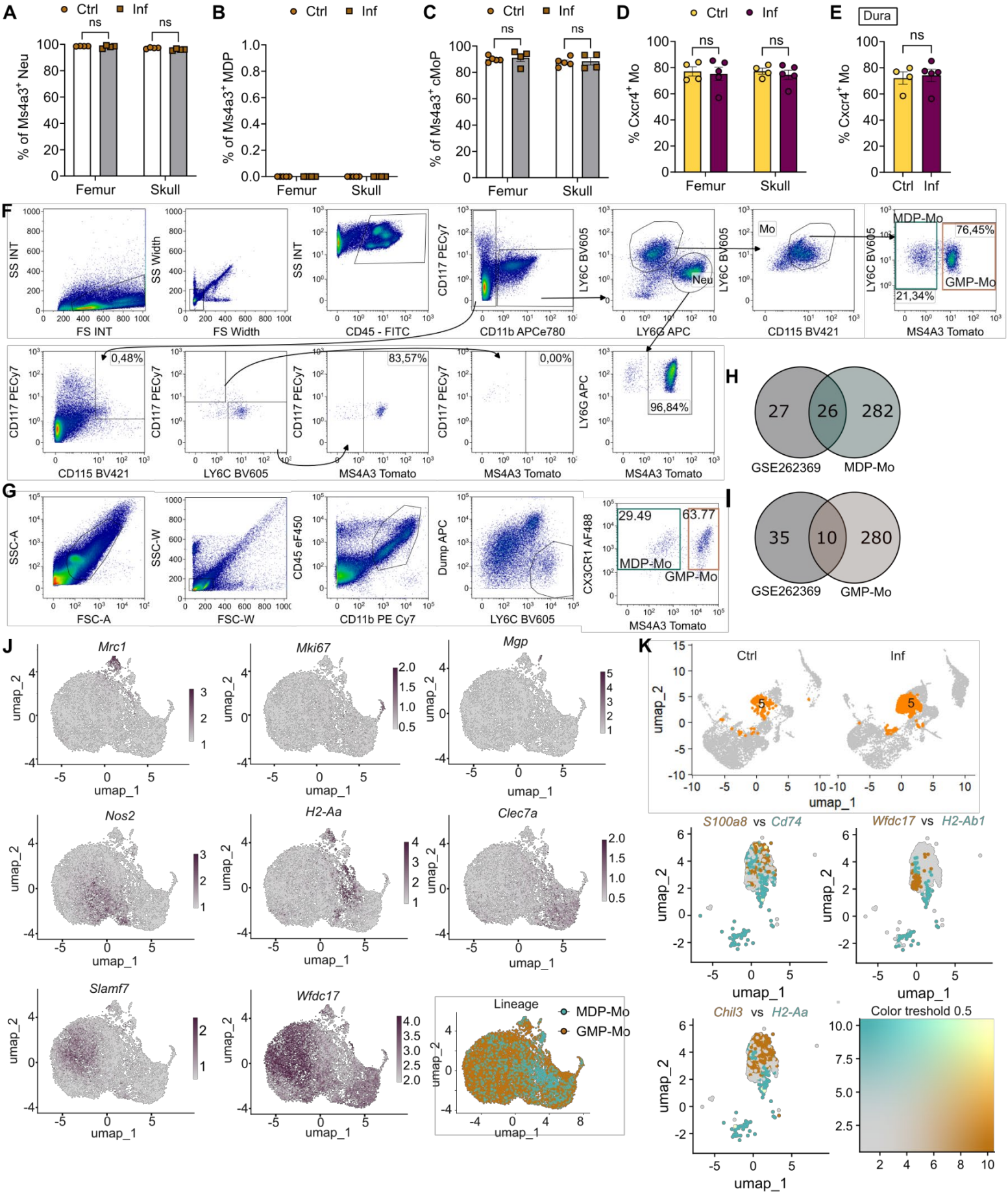

261 **Fig. S6: A-C:** Percentages of Tomato-positive neutrophils (Neu) (**A**), MDP (**B**) and cMoP (**C**) in
262 *Ms4a3^{Cre};R26^{Tomato}* mice in skull and femur, in steady state or 2 dpi. n=4-5, from 2 experiments. Two-way
263 ANOVA and Šídák's multiple comparisons test.**D:** Percentages of Tomato-positive monocytes (Mo) from
264 skull or femur of *Cxcr4^{CreERT2};R26^{Tomato}* mice in steady state or 2 dpi. n=4-5, from 2 experiments. Two-way
265 ANOVA and Šídák's multiple comparisons test. **E:** Percentages of Tomato-positive monocytes from dura of

Cxcr4^{CreERT2};*R26*^{Tomato} mice in steady state or 2 dpi. n=4-5, from 2 experiments. Unpaired t-test. **F-G:** Gating strategy for analysis in skull and femur (**F**) or dura (**G**) from *Ms4a3*^{Cre};*R26*^{Tomato} mice. Plots represent infected skull (**F**) and infected dura (**G**). **H:** Venn diagram comparing DEG from (*40*)(MDP-Mo isolated from steady state bone marrow) and MDP-Mo DEG from pseudobulk anaylsis from infected dura. DEG are defined as padj<0.05 and $\log_2$(fold change)>0.5. **I:** Venn diagram comparing DEG from GSE262369 (GMP-Mo isolated from steady state bone marrow) and GMP-Mo DEG from pseudobulk anaylsis from infected dura. DEG are defined as padj<0.05 and $\log_2$(fold change)>0.5. **J:** Feature plots showing expression of genes specifically upregulated in certain cluster areas. **K:** Upper left: UMAP highlighting cluster 5 in control and infected dura samples (corresponding to Fig. 2). Upper right and bottom panels: Feature plots showing the expression of selected genes differentially upregulated in GMP-Mo (orange) or MDP-Mo (blue) within cluster 5.

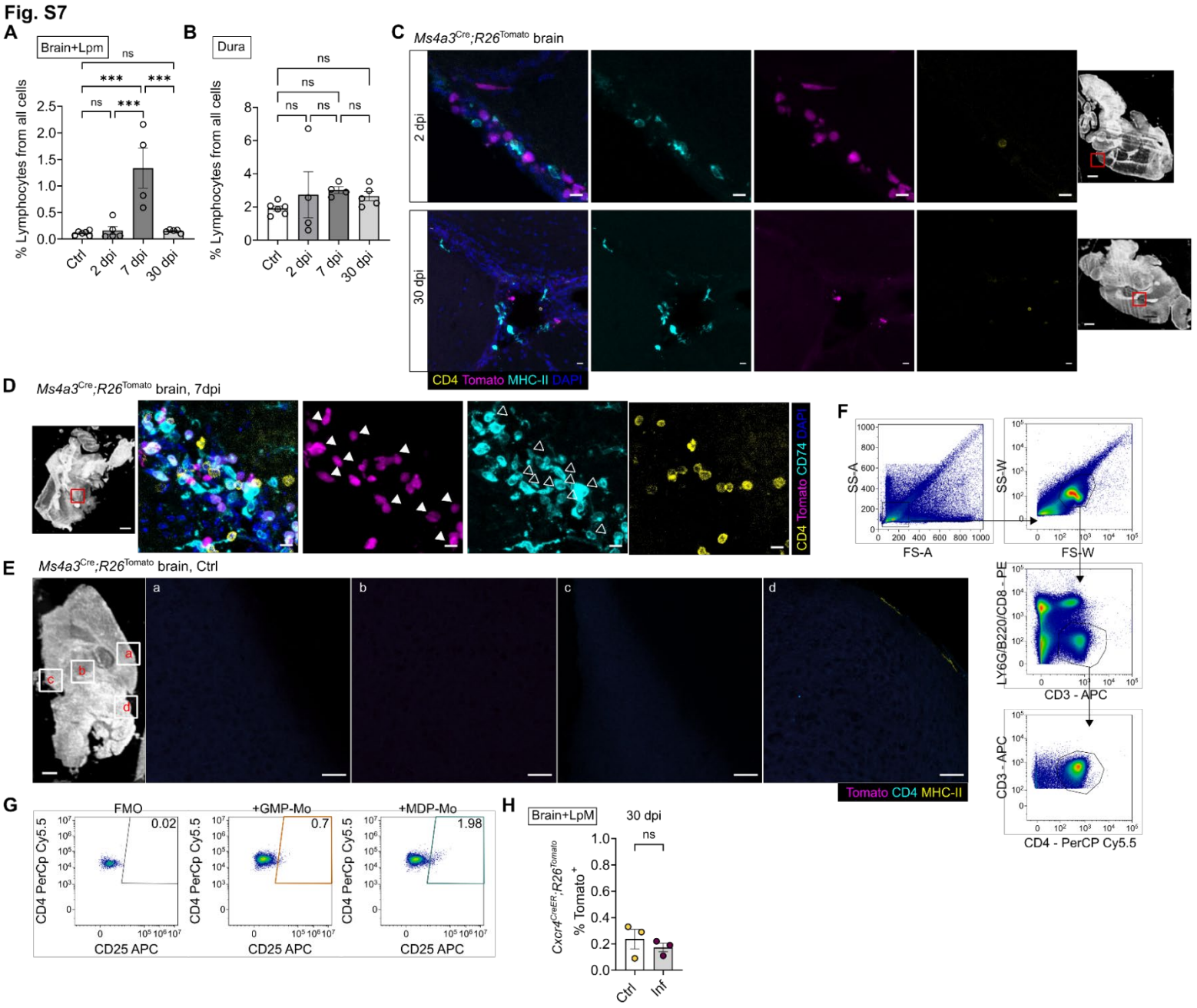

Fig. S7: A-B: Flow cytometry analysis of the percentage of CD11b^{neg}, CD45^{+} lymphocytes in brain (**A**) and dura (**B**). One-way ANOVA, followed by Tukey's test. n=4-5, from 2 experiments. **C:** Representative microscopy images showing brain at 3 dpi and 30 dpi, from *Ms4a3^{Cre};R26^{Tomato}* mice. Positions represented are those where many CD4 T cells are found at 7 dpi, shown or right with red square. Scale bar = 10 µm, scale bar (overview image)= 1000 µm. **D:** Representative microscopy images from brain of *Ms4a3^{Cre};R26^{Tomato}* mouse showing brain at 7 dpi. Anatomical location marked with red square on the overview image (scale bar = 1000 µm). CD74 was used to discriminate between MDP-Mo and GMP-Mo, however, it is not a completely discriminatory marker. The full arrows point to Ms4a3^{+}CD74^{+} cells, while the empty arrows point to cells that are Ms4a3^{neg}CD74^{+}, presumably MDP-Mo. Scale bar = 10 µm. **E:** Representative image of control brain from *Ms4a3^{Cre};R26^{Tomato}* mouse. Letters on the overview image (left, scale bar= 1000 µm) represent anatomical location of magnified images on the right (scale bar=50 µm). **F:** Representative gating strategy for CD4 T cell sorting from cervical lymph nodes. **G:** Representative flow cytometry plots of CD25 in CD4 T cells. **H:** Percentages of Tomato-positive microglia at 30 dpi, from *Cxcr4^{CreERT2};R26^{Tomato}* mice. Student t-test, n=3, from 2 experiments.

Data file S1. Complete list of GO Terms from MDP-Mo and GMP-Mo GO Terms for biological processes, with exclusions of the genes overlapping with GSE262369.

Data file S2. Raw data file